Environment International 213 (2026) 110337

Contents lists available at ScienceDirect

Environment International

journal homepage: www.elsevier.com/locate/envint

Full length article

PFAS exposure modulates mitochondrial susceptibility in steatotic hepatocytes

João Marcos G. Barbosa [a,1], Andi Alijagic [a,b,c,1], Anh Hoang Nguyen [a,c], Victor Castro-Alves [a,d], Lorane Valgueblasse [e], Matej Orešič [c,f,g], Tuulia Hyötyläinen [a,*]

[a] Man-Technology-Environment (MTM) Research Centre, School of Science and Technology, Örebro University, 702 81 Örebro, Sweden
[b] Inflammatory Response and Infection Susceptibility Center (iRiSC), Faculty of Medicine and Health, Örebro University, 702 81 Örebro, Sweden
[c] School of Medical Sciences, Örebro University, 702 81 Örebro, Sweden
[d] Food and Health Centre, Örebro University, 702 81 Örebro, Sweden
[e] École Nationale Supérieure de Chimie de Rennes, Université de Rennes 35700 Rennes, France
[f] Turku Bioscience Centre, University of Turku and Åbo Akademi University, 20520 Turku, Finland
[g] Department of Life Technologies, University of Turku FI-20014 Turku, Finland

ARTICLE INFO

Keywords:
Hepatocytes
Liver diseases
Lipidomics
Metabolomics
PFAS
Steatosis

ABSTRACT

Per- and polyfluoroalkyl substances (PFAS) are highly persistent environmental pollutants that bioaccumulate in living organisms and are increasingly implicated in metabolic dysfunction-associated steatotic liver disease (MASLD). Mitochondria, as central regulators of energy and lipid metabolism, represent key subcellular targets of PFAS toxicity. While emerging studies have examined PFAS-induced mitochondrial dysfunction using whole-cell analyses, studies focusing on mitochondria-enriched cellular fractions and their functional alterations under steatotic conditions, despite their clinical significance, remain limited. Here, we analyzed mitochondria-enriched cellular fractions and the extracellular secretome from human HepaRG hepatocytes exposed to a PFAS mixture under both steatotic and non-steatotic conditions by using liquid chromatography coupled to high-resolution mass spectrometry (LC-HRMS). The PFAS mixture composition and concentrations reflected those commonly reported in human epidemiological data. We observed PFAS- and steatosis-driven effects on metabolism, including lipid buildup in mitochondria-rich fractions due to mitochondrial-lipid droplet contact, disturbances in cardiolipin levels, and increased extracellular abundance of acylcarnitines. Notably, PFAS-induced impact on mitochondrial metabolism was exacerbated in steatotic hepatocytes. Pathway analysis identified disturbances in lipid metabolism and inflammation-related pathways, including leukotriene metabolism, squalene and cholesterol biosynthesis, highlighting a shared metabolic signature across the PFAS-steatosis axis. Functional mitochondrial assays further showed that PFAS exposure suppressed respiratory capacity under both conditions, whereas steatosis alone increased basal mitochondrial activity but nearly abolished spare respiratory capacity. Together, these findings indicate that steatosis is associated with greater PFAS-related alterations in mitochondrial respiration and metabolic composition within the mitochondria-enriched fraction, supporting heightened susceptibility of steatotic hepatocytes to acute PFAS exposure.

1. Introduction

The exceptional physicochemical persistence of per- and polyfluoroalkyl substances (PFAS) makes them useful for a variety of industrial products, yet these characteristics also promote their bioaccumulation. PFAS are widespread in the environment, detectable in the soil (Brusseau et al., 2020), water (Kurwadkar, 2022), air (Morales-McDevitt, 2021), plants (Li et al., 2022), wildlife (Soerensen et al., 2024), and humans (De Silva, 2021), raising significant global concerns for environmental and human health. In humans, PFAS exposure has been associated with various adverse health effects, such as an increased risk of liver damage and the metabolic dysfunction-associated steatotic liver disease (MASLD) (Salihovic, 2018; Momo et al., 2024; Zhang, 2024). PFAS exposure especially impacts hepatocytes, the

* Corresponding author at: School of Science and Technology, Örebro University, 70182 Örebro, Sweden.
E-mail address: tuulia.hyotylainen@oru.se (T. Hyötyläinen).
[1] These authors share first authorship.

https://doi.org/10.1016/j.envint.2026.110337
Received 23 January 2026; Received in revised form 5 May 2026; Accepted 28 May 2026
Available online 29 May 2026

primary functional cells of the liver (Alijagic, 2024). The effects of PFAS in vivo have been linked with the activation of peroxisome proliferator-activated receptors alpha and gamma (PPARα and PPARγ) (Evans, 2022), resulting in changes in hepatic lipid metabolism that disrupt lipid processing and trigger a cascade of molecular events that can lead to hepatic steatosis (Yang, 2023). Although the molecular mechanisms behind PFAS exposure and hepatic lipid metabolism are not yet fully understood, previous studies identified mitochondria as a key target, indicating that PFAS induce metabolic disturbances by impairing mitochondrial function and disrupting membrane potential through increased oxidative stress (Alijagic, 2024; Liu, 2023; Peng, 2013; Huang, 2013).

Mitochondrion is a highly dynamic organelle that plays a crucial role in regulating cellular metabolism by detecting and responding to changes in the cellular environment. These organelles are vulnerable to damage and highly responsive to environmental pollutants (Li et al., 2023; Reddam et al., 2022; Naviaux, 2020). Exposure to environmental pollutants can disrupt mitochondrial metabolic signaling, leading to an abnormally persistent activation of the cell danger response (CDR) and to a hypersensitive cellular state that impacts the immune system and raises the risk of developing metabolic disorders (Naviaux, 2020; Suzuki et al., 2020). Mitochondria are especially sensitive to environmental pollutants due to the pH and membrane potential gradient that drives xenobiotic accumulation, as well as the bioactivation of otherwise inert chemicals by cytochrome P450 enzymes (Meyer, 2013; Roubicek and de Souza-Pinto, 2017).

Several mitochondrial biomarker candidates for early detection of pollutant-induced mitochondrial dysfunction have been proposed (Reddam et al., 2022). For instance, changes in mitochondrial DNA copy number (mtDNAcn), heteroplasmy in mtDNA, 8-hydroxy-2́-deoxyguanine (8-OHdG) as a marker of free radical-induced mtDNA damage, fluctuations in $Ca^{2+,}$ reactive oxygen species (ROS), and adenosine triphosphate (ATP) levels, along with emerging mitochondrial markers such as cell-free mitochondria, mtDNA, and cardiolipin levels, have been proposed as biomarkers of mitochondrial impairment caused by environmental pollutants (Reddam et al., 2022). Nevertheless, current knowledge is limited, and comprehensive metabolomics and lipidomics approaches are needed to elucidate the molecular mechanisms and signatures underlying environmental pollutant–induced (*e.g.,* PFAS) mitochondrial dysfunction.

Exposure to PFAS mixtures in an *in vivo* model caused significant changes in mitochondrial membrane potential and the transcription of genes involved in the respiratory chain, leading to mitochondrial dysfunction as well as disrupting glucose and lipid metabolic pathways (Liu, 2023). Disruption of the lipid metabolism has also been demonstrated *in vitro* on perfluorooctanoic acid (PFOA)-induced hepatotoxicity, which has shown a disturbance in mitochondrial carnitine metabolism, highlighted by an increase in carnitine consumption and acylcarnitine formation (Peng, 2013). Furthermore, our recent study using morphological profiling by cell painting combined with liquid chromatography-high-resolution mass spectrometry (LC-HRMS) analysis of PFAS-exposed HepG2 and HepaRG hepatocytes also showed that changes in the structure and function of mitochondria in the exposed cells might be linked to an increase in the oxidative stress response (Alijagic, 2024). Although recent data indicate that PFAS interact with mitochondria and cause significant changes in the metabolome, previous research has primarily focused on the effects of PFAS exposure at the whole-cell or secretome (*e.g.*, biofluids) level, and data on the mitochondria-enriched fraction are lacking. In addition, despite the high prevalence of MASLD, little is known about how PFAS affect mitochondrial metabolism under steatotic conditions. This knowledge gap limits mechanistic insight into PFAS-induced mitochondrial damage and hinders the identification of standardized mitochondrial markers for early detection and risk assessment.

Here, we performed a comprehensive metabolic analysis to characterize acute metabolic perturbations in HepaRG steatotic and non-steatotic hepatocytes exposed to a PFAS mixture at levels commonly reported in epidemiological studies of various human populations. HepaRG is considered a surrogate for human primary hepatocytes, with preserved metabolic capacity, and shows high correlation with human hepatotoxicity data (Louisse, 2023). The PFAS mixture consisted of perfluorooctanesulfonic acid (PFOS), PFOA, perfluorohexanesulfonic acid (PFHxS), perfluorodecanoic acid (PFDA), and perfluorononanoic acid (PFNA). An *in vitro* early MASLD-like steatosis model was investigated by exposing the HepaRG cell line to saturated (palmitic acid) and unsaturated (oleic acid) fatty acids to induce lipid overload (Gómez-Lechón, 2007). LC-HRMS-based metabolomics and lipidomics were employed to characterize key mitochondrial pathways at the organelle-enriched level, thereby providing deeper insight into the impact of PFAS exposure on mitochondrial health.

2. Materials and methods

2.1. Chemicals

LC-MS grade solvents were purchased from Fisher Scientific (Waltham, MA, USA) and Sigma-Aldrich (St. Louis, MO, USA). MS grade ammonium acetate and formic acid were also purchased from Sigma Aldrich (St. Louis, MO, USA). The lipid standards were obtained from Avanti Polar Lipids Inc. (Alabaster, AL, USA) and Larodan AB (Solna, Sweden). ^{13}C-labeled and native standards, including perfluorocarboxylic acids (PFCAs) and perfluorosulfonic acids (PFSAs), were purchased from Wellington Laboratories (Guelph, Ontario, Canada). Cardiolipin solution from bovine heart was purchased from Sigma-Aldrich (C1649, St. Louis, MO, USA). Native bile acids standards were purchased from Sigma-Aldrich (St. Louis, MO, USA), Steraloids (Newport, RI, USA), Calbiochem (Gibbstown, NJ, USA), and Fluka (Buchs, Switzerland). Bile acids deuterated internal standards (IS) were obtained from Qmx Laboratories Ltd. (Essex, UK). Standard Reference Materials (SRMs) 1950 and 1957 were obtained from the National Institute of Standards and Technology (NIST), U.S. Department of Commerce (Washington, DC, USA). PFAS compounds were obtained from Sigma-Aldrich (St. Louis, MO, USA) with the following purities and ordering numbers: PFOS (98%, 77282), PFOA (98%, 77262), PFHxS (98%, 50929), PFDA (98%, 177741), and PFNA (97%, 394459).

2.2. Preparation of PFAS, palmitic and oleic acid stock solutions

The PFAS ratio in the mixture was determined based on their detected levels in human studies (Alijagic, 2024), specifically: 47.8% PFOS, 28.7% PFOA, 12.1% PFHxS, 6.3% PFDA, and 5.1% PFNA. The PFAS mixture stock solution was prepared by dissolving each compound in dimethyl sulfoxide (DMSO, 99.9%, Sigma Aldrich, Stockholm, Sweden) until reaching the following individual concentrations: 5.20 mg mL^{-1} (PFOS), 3.12 mg mL^{-1} (PFOA), 1.32 mg mL^{-1} (PFHxS), 0.68 mg mL^{-1} (PFDA), and 0.56 mg mL^{-1} (PFNA). For cell exposure, this stock solution was diluted in culture medium to yield final well concentrations of 10.73 μmol L^{-1} PFOS, 6.44 μmol L^{-1} PFOA, 2.72 μmol L^{-1} PFHxS, 1.14 μmol L^{-1} PFDA, and 1.41 μmol L^{-1} PFNA (22.44 μmol L^{-1} total PFAS), with a final DMSO concentration of 0.1% (v/v) in all conditions, including controls. In addition, no major reduction in nuclei count, used as a proxy for cell viability, was observed at the 22.44 μmol L^{-1} PFAS concentration (Fig. S1). This final PFAS mixture concentration was selected for its demonstrated significant impact on mitochondrial phenotypic characteristics (Alijagic, 2024). Palmitic and oleic acids were prepared in a 1:2 (palmitate: oleate) ratio, as this ratio is considered protective in lipotoxic models used in *in vitro* steatosis studies (Gómez-Lechón, 2007; Penke, 2017; Campos-Espinosa and Guzmán, 2021). A stock solution of palmitic acid and oleic acid, both with purity $\geq$ 99% and purchased from Sigma-Aldrich (St. Louis, MO, USA), was prepared in DMSO containing 250 mmol L^{-1} of palmitic acid and 500 mmol L^{-1} of oleic acid, and diluted in culture medium to final well

concentrations of 250 μmol L^{-1} palmitic acid and 500 μmol L^{-1} oleic acid in the wells (0.1% DMSO, v/v, in all conditions).

2.3. Cell culture, seeding, exposure, and sample collection

The HepaRG® human hepatic cell line (Biopredic, France), derived from a female donor, was cultured in basal hepatic cell medium supplemented with HepaRG® Growth Medium Supplement and antibiotics (Biopredic, France). After thawing, cells were cultured in T75 flasks until they reached full confluence (3 to 4 days). Then, the cells were maintained in the same culture flask for 14 days to promote differentiation into hepatocyte-like and biliary-like cells without DMSO (Rose, 2022). Cell culture medium was refreshed every 2–3 days, and the cells were maintained at 37 °C in a 5% CO_2 atmosphere. After 14 days, cells were trypsinized and seeded in 24-well culture plates (VWR, Sweden) at a high density of 10^6 cells per well in a volume of 500 μL and incubated for 24 h. The next day, cells were exposed to the following conditions: i) control, non-exposed, ii) exposed to palmitic and oleic acid in a 1:2 (palmitate: oleate) ratio, iii) exposed to PFAS mixture, and iv) a combination of PFAS mix + palmitate: oleate (1:2) exposure. The final DMSO concentration in the wells was set at 0.1% (v/v). After 24 h of exposure, 300 μL of culture supernatants were collected and stored at − 80 °C, while the remaining supernatants were discarded. 300 μL of pre-warmed PBS was added to each well, and cells were gently scraped and transferred to 96-well deep-well microplates and stored at − 80 °C until extraction and metabolomic analysis to capture acute metabolic perturbations across the exposures. Experiments were performed in three independent biological replicates, each with four technical replicates per condition; the biological replicate served as the primary statistical unit, and technical replicates were used to assess within-experiment reproducibility.

2.4. Nile Red staining and high-content imaging

Nile Red staining was performed to assess intracellular lipid accumulation in HepaRG cells. In brief, cells were seeded in PhenoPlates™ 96-well black-walled microplates (Revvity) at a density of 40 000 cells per well in a final volume of 100 μL. The following day, the cells were exposed to four experimental conditions: i) control (non-exposed), ii) palmitic and oleic acid in a 1:2 (palmitate:oleate) ratio, iii) PFAS mixture, and iv) PFAS mixture combined with palmitate:oleate (1:2). The final well concentrations were 250 μmol L^{-1} palmitic acid and 500 μmol L^{-1} oleic acid for the fatty acid exposures, and 10.73 μmol L^{-1} PFOS, 6.44 μmol L^{-1} PFOA, 2.72 μmol L^{-1} PFHxS, 1.14 μmol L^{-1} PFDA, and 1.41 μmol L^{-1} PFNA (22.44 μmol L^{-1} total PFAS) for the PFAS mixture (0.1% DMSO, v/v, in all conditions). The final volume in each well was adjusted to 200 μL.

After exposure, cells were gently washed twice with PBS to remove residual serum lipids. A Nile Red working solution (1 μg mL^{-1}; Cat. No. N1142, Invitrogen) was prepared by diluting the stock solution (prepared in DMSO) in PBS. Cells were incubated with the Nile Red working solution for 15 min at 37 °C, protected from light. In parallel, nuclear staining was performed using Hoechst 33,342 (Thermo Scientific; 1 μg mL^{-1}). Following incubation, the cells were washed twice with PBS to remove excess dye and subsequently fixed with 4% formaldehyde (Thermo Scientific, Cat. No. 28908) for 10 min at room temperature. Finally, the cells were washed again with PBS at room temperature prior to imaging. Fluorescence imaging was performed using the InCell 2200 High-Throughput Imaging System (GE Healthcare, Uppsala, Sweden) equipped with a 20 × objective.

2.5. Mitochondrial functional analysis

Cells were cultured and differentiated for 14 days as described above, then seeded in 12-well plates under the same ratios and concentrations and exposed to the conditions described in the sections above. After 24 h of exposure, cells were harvested and reseeded at a density of 30 000 cells per well into Agilent Seahorse XFp Poly-D-Lysine–coated Miniplates (Cat. No. 103722–100, Agilent Technologies). This reseeding step was performed to ensure consistent cell numbers across conditions, as PFAS or fatty acid exposures could potentially affect proliferation or induce cytotoxicity, thereby influencing mitochondrial readouts. Therefore, mitochondrial functional analysis should be interpreted as reflecting post-reseeding mitochondrial states that remain distinguishable across exposure groups, rather than as a direct measure of the immediate post-exposure condition.

After incubation for 24 h to allow cell adherence, mitochondrial respiration was assessed using the Agilent Seahorse XFp Cell Mito Stress Test Kit (Cat. No. 103010–100, Agilent Technologies) following the manufacturer's instructions. The assay measures oxygen consumption rate (OCR) in real time to evaluate key mitochondrial function parameters, including basal respiration, ATP-linked respiration, proton leak, maximal respiration, and spare respiratory capacity. Values for all measured parameters were normalized to total protein content.

2.6. Isolation of mitochondria-enriched fraction

The mitochondria-enriched fraction was isolated from cells using the MITOISO2 kit (Sigma-Aldrich, Schnelldorf, Germany) following the detergent lysis method. In summary, the extraction buffer A (Component E2778, Sigma-Aldrich, Schnelldorf, Germany) was diluted 5x in LC-MS-grade water (Fisher Scientific, Waltham, MA, USA), and the protease inhibitor cocktail (Component P8340, Sigma-Aldrich, Schnelldorf, Germany) was added to a final dilution of 1:100 (v/v). The lysis buffer was prepared by diluting the cell lysis solution (Component C1242, Sigma-Aldrich, Schnelldorf, Germany) in a 1:200 (v/v) proportion with extraction buffer A. Then, the cell lysis procedure was performed by adding 100 μL of lysis buffer to each well, followed by incubation on ice for 5 min. The neutralization step was performed by adding 200 μL of extraction buffer A per well, followed by low-speed centrifugation (600 × g) for 10 min at 4 °C. The supernatants were carefully transferred to new cold tubes for high-speed centrifugation (15,000 × g) for 10 min at 4 °C. The pellets (mitochondria-enriched fraction) were then homogenized by adding 150 μL of 0.9% NaCl solution, vortexed, and ultrasonicated for 3 min, then immediately used for metabolites/lipids extraction.

2.7. Polar and semipolar metabolite extraction

For the extraction of polar and semipolar metabolites, 40 μL of the mitochondrial enrichment extract and 60 μL of the cell media was transferred to a 96-well plate, followed by the addition of 480 μL of MeOH:MTBE:IPA (20:15:15, v/v/v) containing the IS mixture (Succinic acid-d4, Glutamic acid-d5, Tryptophan-d5, hexanoic acid-d3, M3PFHxS, GUDCA-d4, GCA-d4, UDCA-d4, CA-d4, MPFNA, M8PFOS, GDCA-d4, CDCA-d4, DCA-d4, GLCA-d4, TCA-d4, M7PFUdA, LCA-d4, and Heptadecanoic acid). The extraction blank was prepared by mixing 40 μL of the 0.9% NaCl solution with 480 μL of the MeOH:MTBE:IPA (20:15:15, v/v/v) IS mixture. The contents of each well were mixed with the pipette and then left to stand on an ice plate in the orbital shaker for 60 min. The extracts were transferred to a 96-well filter plate and filtered using the Biotage PRESSURE + positive manifold (Biotage, Uppsala, Sweden). The filtered extracts were then evaporated and reconstituted in 50 μL of MeOH:H_2O (7:3, v/v). Calibration curves for PFAS (3.75–120 ng mL^{-1}), and polar and semi-polar metabolites (0.10–80 μg mL^{-1}) were run within the batch. The PFAS calibration standards included PFOS, PFOA, PFHxS, PFDA, and PFNA. Quantification was based on transitions of the molecular anion [M − H] − for PFCAs and [M] − for PFSAs, along with one product ion ([M − COOH] − for PFCAs and [FSO_3] − for PFSAs). An additional 1–2 product ions served as qualification ions. The calibration curves for polar and semipolar metabolites included the following metabolites: 2-hydroxybutyric acid, 3-hydroxybutyric acid, alanine,

arachidonic acid, asparagine, aspartic acid, cholesterol, citric acid, fructose, fumaric acid, glutamic acid, glutamine, glycerol-3-phosphate, glycine, indole-3-propionic acid, isoleucine, lactic acid, leucine, linoleic acid, lysine, malic acid, methionine, oleic acid, ornithine, palmitic acid, phenylalanine, proline, serine, threonine, stearic acid, succinic acid, and valine.

2.8. Tricarboxylic acid (TCA) cycle metabolite extraction

The TCA cycle metabolites were extracted using the 3-nitrophenylhydrazine (3-NPH) derivatization method described by Dei Cas et al. (Dei Cas, 2020), with modifications. Briefly, 50 μL of the enriched mitochondrial extract was transferred to a new 96-well plate, and then 20 μL of the IS solution containing the following compounds was added: Acetic acid-d_4, butyric acid-d8, hexanoic acid-d3, and succinic acid-d4. Next, 75 μL of the derivatization mix consisting of 50 mmol L^{-1} of 3-nitrophenylhydrazine (3-NPH), 50 mmol L^{-1} of N-(3-dimethylaminopropyl)-N'-ethylcarbodiimide hydrochloride (EDC), and 7% pyridine, all in MeOH:H_2O (7:3, v/v), was added to each well. The 96-well plate was then incubated on an orbital shaker at 150 rpm for 60 min at room temperature. After incubation, 50 μL of a 0.2% formic acid solution in MeOH:H_2O (7:3, v/v) was added to stop the derivatization reaction, and the samples were transferred to a filtration plate and filtered using the Biotage PRESSURE+ (Biotage, Uppsala, Sweden) positive manifold. The filtrate was collected in a new 96-well plate and immediately analyzed. Calibration curves for the TCA cycle metabolites were prepared and run within the batch, including the following metabolites (0.16–25 ppm): Isovaleric acid, lactic acid, fumaric acid, pyruvic acid, malic acid, 3-hydroxybenzoic acid, valeric acid, 2-ketoglutaric acid, hexanoic acid, butyric acid, 2-hydroxybutyric acid, aspartic acid, isocritric acid, aconitic acid, 3-hydroxybutyric acid, citric acid, succinic acid, glycolic acid, propionic acid, and acetic acid.

2.9. Lipid extraction

For the extraction of the molecular lipids, 40 μL of the mitochondria-enriched fraction homogenate and 60 μL of the cell media was mixed with 480 μL MeOH:MTBE:IPA (20:15:15, v/v/v) containing the following IS (c = 2.5 μL mL^{-1}): 1-heptadecanoyl-2-hydroxy-*sn*-glycero-3-phosphocholine (LPC(17:0)), N-heptadecanoyl-D-*erythro*-sphingosylphosphorylcholine (SM(d18:1/17:0)), N-heptadecanoyl-D-*erythro*-sphingosine (Cer(d18:1/17:0)), 1,2-diheptadecanoyl-*sn*-glycero-3-phosphocholine (PC(17:0/17:0)), 1,2-diheptadecanoyl-*sn*-glycero-3-phosphoethanolamine (PE(17:0/17:0)), 1,2-nonadecanoyl-*sn*-glycero-3-phosphocholine (PC(19:0/19:0)), glyceryl-tripentadecanoate (TG(15:0/15:0/15:0)), cholesteryl-heptadecanoate (CE(17:0)), glyceryl-triheptadecanoate (TG(17:0/17:0/17:0)), and glyceryl trinonadecanoate (TG(19:0/19:0/19:0)). The samples were mixed with the pipette tip, incubated on ice plate in the orbital shaker for 60 min. Then, 420 μL of the extracts were transferred to a filter tube, and after filtration, 100 μL were transferred to a new plate and stored at −80 °C until analysis.

Lipid-class calibration curves were prepared using the following lipids: 1-hexadecyl-2-(9Z-octadecenoyl)-*sn*-glycero-3-phosphocholine (PC(16:0e/18:1(9Z))), 1-(1Z-octadecenyl)-2-(9Z-octadecenoyl)-*sn*-glycero-3-phosphocholine (PC(18:0p/18:1(9Z))), 1-stearoyl-2-hydroxy-*sn*-glycero-3-phosphocholine (LPC(18:0)), 1-oleoyl-2-hydroxy-*sn*-glycero-3-phosphocholine (LPC(18:1)), 1-palmitoyl-2-oleoyl-*sn*-glycero-3-phosphoethanolamine (PE(16:0/18:1)), 1-(1Z-octadecenyl)-2-docosahexaenoyl-*sn*-glycero-3-phosphocholine (PC(18:0p/22:6)), 1-stearoyl-2-linoleoyl-*sn*-glycerol (DG(18:0/18:2)), 1-(9Z-octadecenoyl)-*sn*-glycero-3-phosphoethanolamine (LPE(18:1)), N-(9Z-octadecenoyl)-sphinganine (Cer(d18:0/18:1(9Z))), 1-hexadecyl-2-(9Z-octadecenoyl)-*sn*-glycero-3-phosphoethanolamine (PE(16:0/18:1)), 1-Palmitoyl-2-Hydroxy-*sn*-Glycero-3-Phosphatidylcholine (LPC(16:0)), 1,2,3 trihexadecanoalglycerol (TG(16:0/16:0/16:0)), 1,2,3-trioctadecanoylglycerol (TG(18:0/18:0/18:0), 3β-hydroxy-5-cholestene-3-stearate (ChoE (18:0)), and 3β-Hydroxy-5-cholestene-3-linoleate (ChoE(18:2)). Lipid identification relied on class-specific calibration standards, retention-time behavior, and MS/MS fragmentation patterns. Species for which acyl-chain composition could be assigned unambiguously were reported at the *sn*-position level, whereas lipids lacking full acyl-chain positional or double-bond information were reported in shorthand sum-composition form. The calibration curves, with a concentration range of 0.1–5.0μL mL^{-1}, presented a linearity (R^2) ranging ≥ 0.99 for the lipids.

2.10. LC-HRMS metabolomic analysis

Four separate analyses were performed: one focused on polar and semipolar metabolites, the second on the derivatization method for TCA cycle metabolites, and two on lipidomics in positive and negative ion modes. All analyses were performed using ultra-high-performance liquid chromatography-quadrupole time-of-flight mass spectrometry (UHPLC-QTOFMS). NIST SRM 1950 and 1957, pooled samples, in-house pooled serum, and extracted blanks were used for quality control (QC) and quality assurance (QA) during the batches. Samples were randomized before UHPLC-QTOFMS analysis.

2.11. LC-HRMS polar and semipolar, and TCA-related metabolomic analysis

The platform used for polar and semipolar compounds, as well as for the TCA cycle metabolites, was an ACQUITY Premier UPLC system (Waters Corporation, Wexford, Ireland) equipped with a multi-sampler organizer (set to 10 °C), column thermostat (kept at 50 °C), sample manager FTN, and binary system manager from Waters (Waters Corporation, Wexford, Ireland), coupled with an Xevo G3 QToF MS system with a dual Zspray electrospray ionization (ESI) source (Waters Corporation, Wexford, Ireland). Data acquisition was done using the vendor software ACQUITY console and MassLynx v4.2 (Waters Corporation, Wexford, Ireland). The chromatographic column used was an ACQUITY UPLC® BEH C18 column (2.1 mm × 100 mm, particle size 1.7 μm) coupled to an ACQUITY UPLC® BEH C18 VanGuard precolumn (5 mm x 2.1 mm, 1.7 μm), both from Waters (Milford, MA, USA).

For polar and semipolar compounds, the following conditions were applied: i) 0.4 mL min^{-1} of flow rate, ii) 1 μL of injected volume for full scan and 2 μL for auto MS/MS acquisition, iii) mobile phase (MP) A consisted of H_2O:MeOH (v/v, 70:30), and the MP B of 100% MeOH, both spiked with 2 mmol L^{-1} of ammonium acetate and 0.1% (v/v) of formic acid, iv) chromatography gradient set as 0–1.5 min (MP B ramped from 5 to 30%), 1.5–4.5 min (MP B increased to 70%), 4.5–7.5 min (MP B increased to 100% and maintained for 5.5 min), 7.5–10 min (MP B returned to initial conditions of 5% and held for 5 min), v) post-time run of 1 min. The MS configuration was: i) negative ESI polarity, ii) 1.5 kV of capillary voltage, iii) sample cone set at 40 V, iv) *m/z* range of 100–1200, v) temperature source of 150 °C, vi) desolvation temperature of 550 °C, vii) cone gas and desolvation gas flow of 50 and 1000 L h^{-1}, respectively, viii) leucine enkephalin (*m/z* 554.2615) as the reference compound for the lockspray, ix) lockspray capillary voltage of 1.5 kV, and x) MS acquisition speed of 0.2 spectra s^{-1}.

For the TCA cycle metabolites, the settings were: i) 0.4 mL min^{-1} of flow rate, ii) 1 μL of injected volume for full scan and 2 μL for auto MS/MS acquisition, iii) MP A consisted of 0.1% (v/v) of formic acid spiked in H_2O, and MP B of 100% of acetonitrile, iv) chromatography gradient starting with 10% of MP B (held for 2 min), and then increasing to 100% of MP B (2 to 4 min, and kept for 2 min), and further re-equilibration to the initial conditions (10% of MP B) for 4 min. The MS was set as follows: i) negative ESI polarity, ii) 3.6 kV of capillary voltage, iii) collision energy of 0 V, iv) *m/z* range of 100–1200, v) temperature source of 150 °C, vi) desolvation temperature of 550 °C, vii) cone gas and desolvation gas flow of 50 and 1000 L h^{-1}, respectively, viii) leucine enkephalin (*m/z* 554.2615) as the reference compound for the lockspray, ix) lockspray

capillary voltage of 1.5 kV, and x) MS acquisition speed of 0.2 spectra s^{-1}.

2.12. LC-HRMS lipidomic analysis

The UHPLC equipment used for lipidomics was a 1290 Infinity II system paired with a 6545 QTOFMS system (Agilent Technologies, Santa Clara, CA, USA), equipped with a dual ESI source. The setup included a multi-sampler (kept at 10 °C), a quaternary solvent manager, a column thermostat (set to 50 °C), and MassHunter B.06.01 software (Agilent Technologies, Santa Clara, CA, USA) for data collection. The column used was an ACQUITY UPLC BEH C18 VanGuard precolumn, an inline filter with a pore size of 0,2 μm (Waters Corporation, Wexford, Ireland), and an ACQUITY UPLC® BEH C18 column (2.1 mm × 100 mm, particle size 1.7 μm) by Waters (Milford, MA, USA). MP A consisted of water, and MP B of acetonitrile: isopropanol (v/v, 1:1), both spiked with 10 mmol L^{-1} ammonium acetate and 0.1% (v/v) formic acid for positive ion mode and spiked with 10 mmol L^{-1} ammonium acetate and 0.1% (v/v) ammonium hydroxide for negative ion mode. The elution gradient was set as follows: i) 0 to 2 min, MP B increased from 35% to 80%, ii) 2 to 7 min, B increased to 100%, iii) 7 to 14 min, held at 100%, and iv) post-run of 7 min for equilibration. The MS conditions were configured with a dual ESI ionization source, using a capillary voltage of 3.64 kV, a nozzle voltage of 1500 V, a N_2 pressure of 21 psi as the nebulizer gas, and a N_2 flow rate and temperature of 11 L min^{-1} and 379 °C, respectively, as the sheath gas. The MS1 acquisition speed was two spectra per second, with an *m/z* range of 100–3000. The auto MS2 *m/z* range used was 50–3000, a fragmentor voltage of 15 V, and collision energies of 20, 30, and 40 eV.

2.13. Data processing

The data processing was performed using the open-source software MZmine (version 4.7.3) (Schmid, 2023) using the following parameters: i) Mass detection noise level: 500, ii) ADAP Chromatogram builder with a minimum 6 consecutive scan, minimum intensity and height of 200 and 500, respectively, and a *m/z* tolerance of 0.006 (*m/z*) or 10 ppm, iii) chromatogram resolving using the local minimum algorithm with a 60% chromatographic threshold, minimum retention time (RT) search range of 0.02, minimum relative height of 5%, absolute height of 400, minimum ration of peak top/edge of 1.05, and a peak duration range of 0.1–1.0, iv) feature list filtering by keeping all the rows with a *m/z* range of 150–1200 (for polar and semipolar compounds and TCA cycle metabolites) and 150–3000 (for lipidomics) from 0.5 up to 12 min, and removing all the rows with a *m/z* ranges of 800–1200 (0.5–4 min) and 370–500 (8–12 min), v) Carbon-13 (^{13}C) filter with a *m/z* and RT tolerance of 5.0 ppm and 0.05 min, respectively, maximum charge of 2, and the most intense isotope as the representative one, vi) Join aligner with a tolerance of 0.009 *m/z*, a RT tolerance of 0.12 min and a weight of 2:1 (*m/z*: RT), and no requirement of same charge state or ID, vii) feature list filtering of minimum of 10% of presence in the samples, viii) Gap filling using the peak finder algorithm set with intensity tolerance of 40%, *m/z* tolerance of 10 ppm, and RT tolerance of 0.20 min, ix) annotation of compounds using an in-house database with an *m/z* tolerance of 10.0 ppm and an RT tolerance of 0.25 min. Lipid and metabolite intensities normalization was performed using internal standards: LPC(17:0), PC(17:0/17:0), Cer(d18:1/17:0), and TG(15:0/15:0/15:0) for lipids, tryptophan-d5, M8PFOS, and heptadecanoic acid for polar and semipolar metabolites, acetic acid-d_5, butyric acid-d8, and succinic acid-d4 for the TCA cycle metabolites. Then, data filtering was performed by retaining compounds with a relative standard deviation (RSD) of less than 30% in the pooled quality control (Pooled QC) samples and a signal-to-noise ratio (S/N) at least 3-fold higher in the samples than in the extraction blanks.

Peak annotation was performed using an in-house chemical standards-based database containing chromatographic (retention time) and spectral data (*m/z*) information, achieving levels 1 and 2 of identification according to the Metabolomic Standard Initiative (MSI) (Salek et al., 2013). Cardiolipin putative annotations were confirmed using MS/MS screening analysis of the commercial cardiolipin solution from bovine heart (C1649, Sigma-Aldrich, St. Louis, MO, USA). In the pooled samples, 51.8% of the annotated lipids, 40.5% of the polar and semipolar compounds, and 34.4% of the derivatized TCA cycle metabolites had an RSD < 10%. Additionally, 30.9% of the annotated lipids, 41.8% of the polar and semipolar compounds, and 37.5% of the derivatized TCA cycle metabolites exhibited RSDs of 10–20%. Lastly, 17.3% of the annotated lipids, 17.7% of the annotated polar and semipolar compounds, and 28.1% of the derivatized TCA cycle metabolites had an RSD between 20% and 30%. Unknown compounds with RSD < 30% after data filtering steps were also retained.

2.14. Data analysis

Data analyses were carried out using the web-based platform software "MetaboAnalyst 6.0 (https://www.metaboanalyst.ca/)" (Pang, 2024), GraphPad Prism software (−v10.4.2, https://www.graphpad.com/), and R statistical programming language (−*v*4.4.1, https://www.r-project.org/) in an RStudio environment (−*v*2024.12.0, https://posit.co/), using the following packages: tidyverse (−*v*2.2.0, https://www.tidyverse.org/), ggraph (−*v*2.2.1, https://ggraph.data-imaginist.com/), igraph (−*v*2.1.4, https://igraph.org/), circlize (−*v0.4.16*, https://jokergoo.github.io/circlize/), and ggplot2 (−*v3.5.1*, https://ggplot2.tidyverse.org/). The lipidomics and metabolomics data were log-transformed (log_{10}) to reduce heteroscedasticity and autoscaled within each dataset. In addition to evaluating each compound as a variable, we also normalized and grouped metabolites and lipids by their respective compound classes based on HMDB and LIPID MAPS classifications (Wishart, 2022; Conroy, 2024). Furthermore, due to the interaction between PFAS exposure and the balance between carnitine (CAR) and acylcarnitine (AC) (Peng, 2013), the AC/CAR class ratio was also used as a variable. To provide a supportive internal assessment of treatment-dependent changes in the composition of the mitochondria-enriched fraction, we calculated lipid-based compositional fractions from the LC-HRMS data using class sums of normalized lipid intensities. The LD-like fraction was defined as $\Sigma TG/(\Sigma TG + \Sigma PC + \Sigma PE + \Sigma PI + \Sigma PS + \Sigma SM + \Sigma CL)$; the ER/MAM-like fraction as $(\Sigma PI + \Sigma PS)/(\Sigma PI + \Sigma PS + \Sigma PC + \Sigma PE + \Sigma CL)$; and the Mito-like fraction as $\Sigma CL/(\Sigma CL + \Sigma PC + \Sigma PE + \Sigma PI + \Sigma PS + \Sigma SM)$. These fractions were used as supportive internal indicators of treatment-dependent changes in fraction composition, rather than as definitive measures of organelle purity. The statistical uni- and multivariate approaches included fold-change (FC) analysis between groups (FC threshold $\geq \pm 1.25$), non-parametric t-tests, principal component analysis (PCA), and Spearman (Partial) correlation for measured PFAS concentrations in the mitochondria-enriched fraction and extracellular media. Unless otherwise specified, significant feature differences are based on nominal *p*-values < 0.05. These univariate analyses were exploratory, focusing on pattern discovery, and were interpreted alongside FCs, consistency across related metabolite or lipid classes, and pathway-level results. The semi-polar, polar, and TCA cycle metabolite datasets, containing annotated and unknown metabolites, were normalized (log_{10}-transformed and autoscaled within each dataset), merged, and uploaded to the functional pathway analysis module of MetaboAnalyst 6.0 (Lu et al., 2023), yielding FC, *p-values*, and false discovery rate (FDR) values. The algorithms Mummichog and Gene Set Enrichment Analysis (GSEA) were applied to assess the relative significance of pathways, using a FDR-corrected p-value cutoff of 0.1, the human-genome-scale metabolic model library (Mummichog package, https://shuzhao-li.github.io/mummichog.org/index.html), and the Kyoto Encyclopedia of Genes and Genomes (KEGG, https://www.genome.jp/kegg/) (Kanehisa et al., 2019). The pathway analysis was conducted with a mass tolerance of 10 ppm and by selecting representative adducts, as isotopic adducts had already been removed during data processing.

3. Results

The study design is shown in Fig. 1. Steatotic and non-steatotic HepaRG hepatocytes were exposed to a PFAS mixture, then analyzed by LC-HRMS-based metabolomics and lipidomics to quantify alterations in mitochondrial pathways using both mitochondria-enriched fractions and extracellular media. This was combined with functional mitochondrial stress testing to study the organelle-level impacts of PFAS-induced metabolic disruption and its interaction with early MASLD-like steatosis. To further characterize the composition of the mitochondria-enriched fraction, we calculated lipid-based compositional fractions from the LC-HRMS lipidomics data (Fig. S2A). Across all groups, the Mito-like fraction remained dominant, consistent with the retention of a cardiolipin-rich mitochondrial lipid signature in the enriched fraction. In contrast, the ER/MAM-like fraction remained uniformly low across groups, indicating that it was not dominated by PI/PS-enriched non-mitochondrial membrane material in this lipid-based compositional analysis. The LD-like fraction was increased in steatosis-containing groups, supporting treatment-dependent TG-associated remodeling of the mitochondria-enriched fraction under lipid overload. Furthermore, we compared the lipid composition of mitochondria-enriched fractions with that of whole-cell HepaRG extracts (Fig. S2B). The Mito-like lipid fraction was significantly more abundant in the mitochondria-enriched samples than in whole cells, whereas the LD-like and ER/MAM-like fractions were significantly reduced. These results indicate that the mitochondria-enriched fraction has a distinct composition compared with whole-cell extracts and is enriched in cardiolipin-related mitochondrial lipids. The PCA plots in Figs. S3–S4 reveal exposure-dependent clustering patterns in the omics data, with notable overlap among groups, whereas the lipidomics datasets, both in extracellular media and mitochondria-enriched fraction, show a modest separation trend.

3.1. Hepatocyte steatosis model reveals mitochondrial lipid remodeling and TCA cycle-associated signatures

In order to characterize the PFAS-induced metabolic fingerprint in steatosis, we conducted a comprehensive LC-HRMS-based omics analysis of mitochondria-enriched fractions and extracellular media from PFAS-exposed HepaRG steatotic and non-steatotic hepatocytes, encompassing polar and semipolar compounds, TCA cycle metabolites, and a wide range of lipids. The identified and annotated metabolites, along

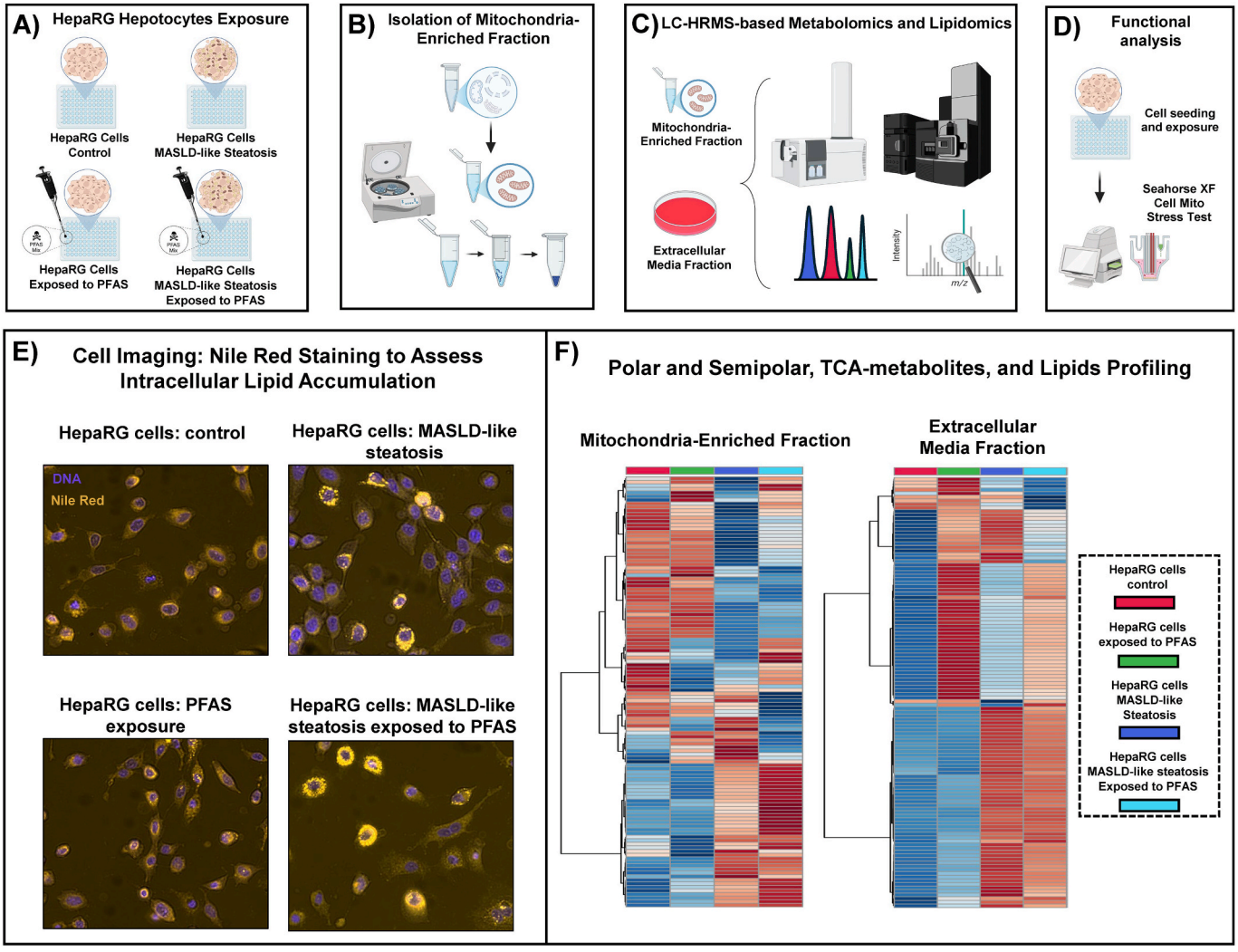

Fig. 1. Study design, lipid labeling, and general metabolomic/lipidomic effects. A) HepaRG hepatocyte exposures, i) Control (non-exposed), ii) MASLD-like induced steatosis, iii) Exposure to PFAS mixture, iv) MASLD-like steatosis combined with PFAS exposure. **B)** Isolation of mitochondria-enriched fraction. **C)** Polar, semipolar, TCA cycle metabolites, and lipids analysis of the mitochondria-enriched and extracellular media fraction by liquid chromatography-high-resolution mass spectrometry (LC-HRMS). **D)** Seahorse XF Cell Mito Stress Test. **E)** Representative cell images of Nile Red lipid staining. **F)** General metabolomics and lipidomics of mitochondrial extracts and extracellular media affected by the exposures. (For interpretation of the references to colour in this figure legend, the reader is referred to the web version of this article.)

with their FC and *p*-values, are listed in Supplementary Table S1 (Table S1). Tables S2 and S3 also show the specific metabolites that exhibit significant correlations within the mitochondria-enriched fraction and the extracellular media fraction. In the mitochondria fraction, the per-well total cell normalized concentration for PFAS was: 0.012 μmol L^{-1} PFOS (RSD: 5.5%), 0.017 μmol L^{-1} PFOA (RSD: 10.7%), 0.021 μmol L^{-1} PFHxS (RSD: 8.6%), 0.017 μmol L^{-1} PFDA (RSD: 7.6%), and 0.017 μmol L^{-1} PFNA (RSD: 25.8%), with no statistically significant differences between the average concentration in the steatotic and non-steatotic conditions. In the extracellular media, the total average normalized concentration for PFAS was: 0.56 μmol L^{-1} PFOS (RSD: 11.3%), 2.03 μmol L^{-1} PFOA (RSD: 11.3%), 6.97 μmol L^{-1} PFHxS (RSD: 7.86%), 13.20 μmol L^{-1} PFDA (RSD: 14.2%), and 0.071 μmol L^{-1} PFNA (RSD: 16.8%). For PFHxS (7.20 and 6.62 μmol L^{-1} average concentration in the non-steatotic and steatotic conditions, respectively) and PFOA (2.15 and 1.86 μmol L^{-1} average concentration in the non-steatotic and steatotic conditions, respectively), a significant concentration decrease was found during the steatotic condition, suggesting a higher intracellular uptake of both compounds during steatosis. Table S4 summarizes the normalized average concentrations of each PFAS in the mitochondria-enriched fraction and in extracellular media.

We first examined the metabolomic and lipidomic profiles in an *in vitro* steatosis model by exposing the HepaRG hepatocytes to palmitate and oleate to induce lipid overload. This model is known to have minimal toxic and apoptotic effects, making it suitable for studying steatosis by replicating key features of MASLD in humans (Gómez-Lechón, 2007). Nile Red staining confirmed increased intracellular lipid accumulation, indicating induction of a steatotic hepatocyte phenotype (Fig. 1). At the metabolite class level, significant decrease (Fig. 2A and B) was observed in the mitochondria-enriched fraction of the HepaRG hepatocyte steatosis model compared to the non-exposed group for the following lipid classes: phosphatidylcholines (PC, FC = -1.57), cholesteryl esters (CE, FC = -1.55), phosphatidylethanolamines (PE, FC = -1.44), sphingomyelins (SM, FC = -1.76); on the other hand, a highly significant upregulation and positive correlation ($p < 0.001$) was found for the triacylglycerols (TG, FC = 1.45) class. Particularly, several TGs, both unsaturated and saturated, were upregulated in the mitochondria-enriched fraction after exposure to palmitic and oleic fatty acids (Fig. 2C).

In the extracellular media of the HepaRG cell steatosis model, nucleotides showed downregulation, while the AC class was particularly upregulated (Fig. 2D, E, and F), which can also be evidenced by the increased ratio of AC/CAR (FC = 1.87). Moreover, in addition to the several ACs species with increased levels in the extracellular media, metabolites related to amino acids as precursors feeding into the TCA cycle, such as 3-methyl-2-oxovaleric acid (FC = 1.71) and hydroxyglutaric acid (FC = 2.77), as well as a β-oxidation intermediate, such as 3-hydroxydecanoic acid (FC = 3.60), also showed an upregulated pattern in the cell media (Fig. 2D,E, and F).

3.2. PFAS exposure is associated with changes in lipids and metabolites in the mitochondria-enriched fraction of hepatocytes

The mitochondria-enriched fraction of the HepaRG hepatocytes exposed to the PFAS mixture showed a significant downmodulation of lysophosphatidylcholine class (LPC, FC = -2.38), in addition to an increase of peptides (FC = 1.66) (Fig. 3A). Interestingly, a lipid from the cardiolipin (CL) class, which is exclusively present in the inner mitochondrial membrane, CL(76:8), also showed a depletion (FC = -2.65) after PFAS exposure (Fig. 3A). In addition, several CLs were correlated with individual PFAS (Table S2), consistent with altered cardiolipin-associated lipid composition within the mitochondria-enriched fraction. By evaluating the interplay between each PFAS with the compound class, a significant positive correlation was observed between PFNA and amino acids and nucleotides (Fig. 3B). Partial Spearman correlation network analysis (Fig. 3C) also showed the overall association of PFAS on polar and semipolar metabolites involved in the mitochondrial respiratory chain, protein synthesis, and TCA cycle metabolites, as well as on several fatty acids, phospholipids, TGs, and mitochondrial lipids (PFAS-cardiolipin correlations).

By investigating the cell media of HepaRG cells exposed to the PFAS mixture, we observed upregulation of several lipids from the PC class (Fig. 3D). For instance, while the PC(38:4) showed a decrease in the mitochondria-enriched fraction (FC = -2.30), this phospholipid was found to increase in the extracellular media (FC = 1.30). This balance can also be demonstrated at the compound class level, as shown by the negative correlation between PFDA and the AC/CAR ratio levels in the mitochondria-enriched fraction (Fig. 3B), contrasting with its positive correlation in the cell media (Fig. 3E). Moreover, the PFAS exposure triggered upregulation of PC, phosphatidylinositol (PI), phosphatidylserine (PS), and SM, in contrast with a negative correlation with TG (Fig. 3E). Notable partial correlations can be observed between PFAS and metabolites, such as amino acids and their derivatives, bile acids (*e.g.*, GDCA and GHCA), PCs, as well as several other phospholipids (Fig. 3F). Importantly, a distinct profile appears in the interaction between PFAS and metabolites/lipids in the mitochondria-enriched fraction compared to the cell media (Fig. 3C,F).

3.3. PFAS exposure significantly impacts mitochondrial metabolism in the hepatocyte steatosis model

In the HepaRG hepatocyte steatosis model exposed to PFAS, a clearly stronger impact on metabolism was observed compared with the steatotic model or PFAS exposure alone. Several lipid classes, such as CE (FC = -1.59), PC (FC = -1.44), SM (FC = -1.66), PE (FC = -1.36), PS (FC = -1.52), and CAR (FC = -2.37) showed significant downregulation, in contrast to upregulation of TG class (FC = 1.40) (Fig. 4A). At an individual metabolite level, lauric acid, deoxyuridine, tyrosine, and L-carnitine showed a decrease in the mitochondria-enriched fraction in the HepaRG steatosis model exposed to PFAS compared to the non-exposed model. Among the increased compounds in the PFAS-exposed steatosis model, the majority were unsaturated and saturated TGs (Fig. 4A).

Moreover, several additional compound classes correlated with each PFAS in the hepatocyte steatosis model (Fig. 4B). Nucleotides showed positive correlations with PFDA, PFHxS, and PFNA. PFNA also showed a slightly positive correlation with amino acids, peptides, and fatty acids. On the other hand, AC showed negative correlations with PFDA, PFHxS, and PFOA, while ceramides (CER) showed negative correlations with PFHxS and PFOA. Positive correlation was found between the LPC class and PFOA. A negative correlation was also seen between PFDA and the AC/CAR ratio. Furthermore, partial correlation analysis (Fig. 4C) indicated a greater impact of PFAS in the steatosis model than in either condition alone, showing a correlation between PFAS and a greater number of metabolites directly involved in the mitochondrial respiratory chain and the TCA cycle. It also revealed greater influence on mitochondrial lipids, as evidenced by more PFAS-cardiolipins associations than in the non-steatosis HepaRG cells model exposed to a PFAS mixture (Fig. 3, Table S2).

In the extracellular media of the steatosis model exposed to the PFAS, CER (FC = 1.40) and AC (FC = 1.37) compound classes were upregulated (Fig. 4DE). Increased extracellular ACs represented the most prominent metabolic signature in this setup, shown also by the increased level of the AC/CAR ratio (FC = 1.72), as well as several upregulated AC compounds, such as palmitoylcarnitine (FC = 2.64), hexanoylcarnitine (FC = 2.62), myristoyl-L-carnitine (FC = 2.47), octadecenoylcarnitine (FC = 2.33), 9-decenoylcarnitine (FC = 1.67), and butyrylcarnitine (FC = 1.30). Other compound classes were associated with PFAS exposure combined with steatosis, as evidenced by positive correlations with amino acids and hydroxy-fatty acids and negative correlations with nucleotides, polyamines, carbohydrates, and LPC. Interestingly, all PFAS showed negative correlations with PCs, and PFHxS showed positive

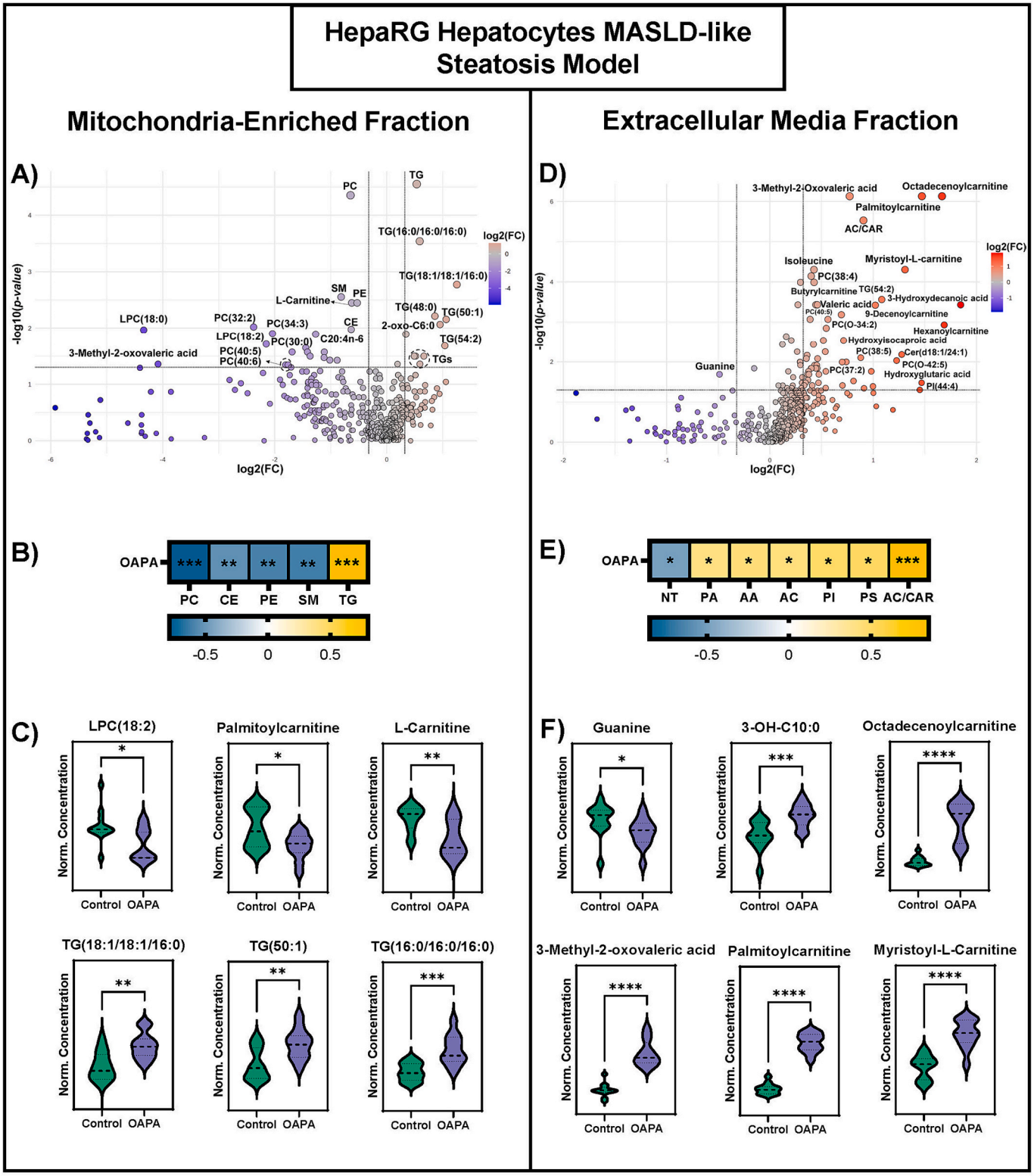

Fig. 2. Steatosis-induced metabolic remodeling in mitochondrial and extracellular fractions. A) Volcano plot showing the significant metabolites, lipids, and compound classes (FC>±1.25, $p < 0.05$) between the mitochondrial-enriched fraction of the HepaRG steatosis model and the control HepaRG model. **B)** Heatmap showing the significant ($p < 0.05$) metabolic patterns between the two mitochondrial-enriched fractions (steatosis x control). **C)** Example of significant metabolites and lipids between the steatosis condition and the control mitochondria-enriched fraction of HepaRG cells. **D)** Volcano plot showing the significant metabolites, lipids, and compound classes (FC>±1.25, $p < 0.05$) between the cell media extract of the HepaRG steatosis model and the control HepaRG model. **E)** Heatmap showing the significant ($p < 0.05$) metabolic patterns between the two cell media extracts (steatosis x control). **F)** Example of significant metabolites and lipids between the steatosis condition and the control cell media of the HepaRG cells. **Abbreviations:** OAPA (Oleic acid, Palmitic acid: steatosis), Phosphatidylcholines (PC), Cholesteryl esters (CE), Phosphatidylethanolamines (PE), Sphingomyelins (SM), Triacylglycerides (TG), Phosphatidylinositol (PI), Phosphatidylserine (PS), Acyl Carnitines (AC), AC/CAR (Acyl Carnitines / Carnitines ratio), Nucleosides and Nucletotides (NT), Polyamines (PA), Amino acids (AA), 2-Ketohexanoic acid (2-oxo-C6:0), 3-Hydroxydecanoic acid (3-OH-C10:0). Level of significance: $*p < 0.05$, $**p < 0.01$, $***p < 0.001$, $****p < 0.0001$.

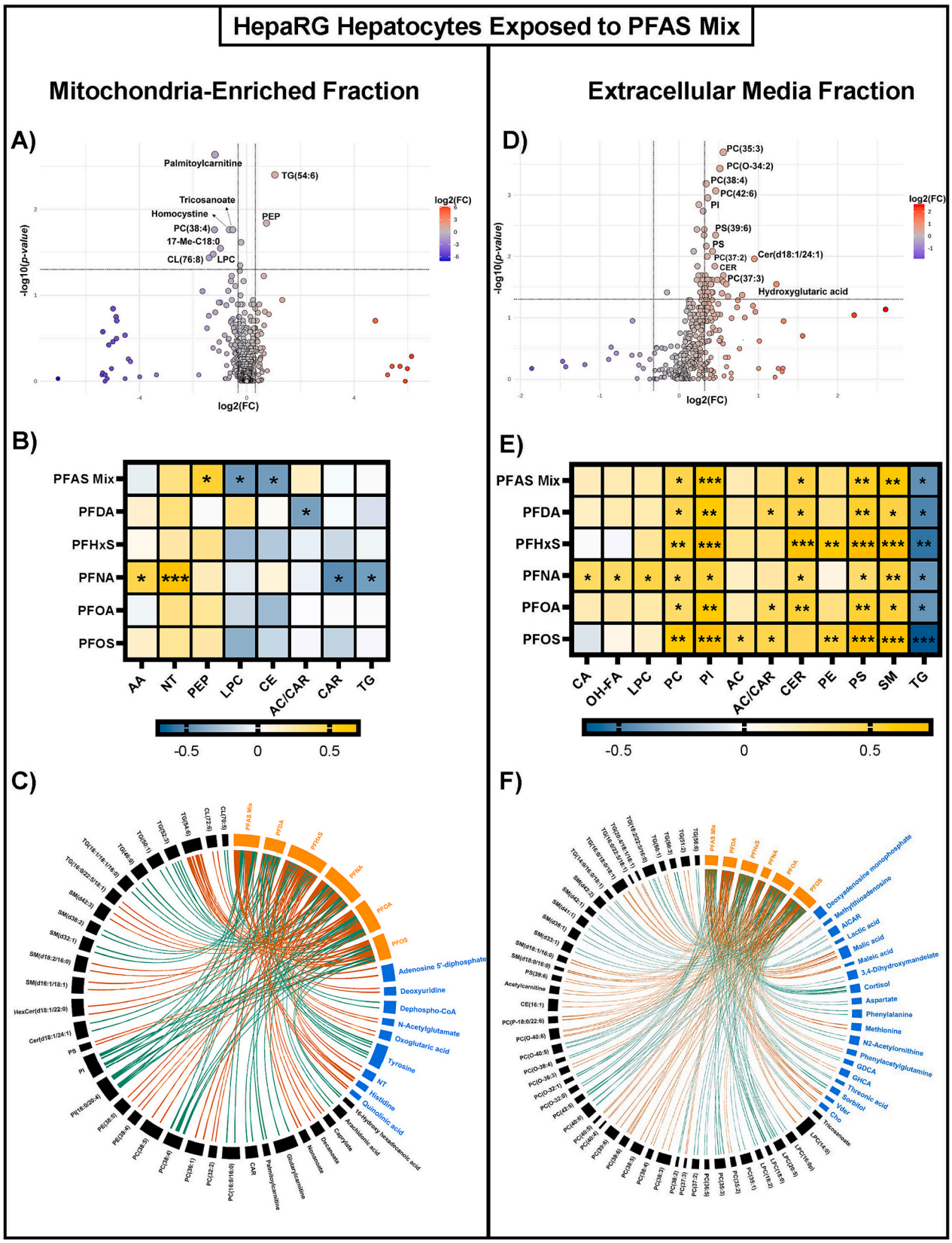

(caption on next page)

Fig. 3. PFAS-induced metabolic remodeling in mitochondrial and extracellular fractions. A) Volcano plot showing the significant metabolites, lipids, and compound classes (FC>±1.25, $p < 0.05$) between the mitochondrial-enriched fraction of the HepaRG cell exposed to the PFAS mix model and the control HepaRG model. **B)** Heatmap showing the significant ($p < 0.05$) metabolic patterns between the two mitochondrial-enriched fractions (PFAS-exposed x control). **C)** Chord plot showing the significant partial (Spearman) correlation between PFAS and the metabolites, lipids, and compound class of the mitochondrial-enriched fraction of HepaRG cells exposed to PFAS. Intra-metabolites, lipids, and compound class correlations have been removed for clarity. The orange color indicates a positive correlation, and the green color represents a negative correlation. **D)** Volcano plot showing the significant metabolites, lipids, and compound classes (FC>±1.25, $p < 0.05$) between the cell media extract of HepaRG cells exposed to the PFAS mix model and the control HepaRG model. **E)** Heatmap showing the significant ($p < 0.05$) metabolic patterns between the two cell media extracts (PFAS-exposed x control). **F)** Chord plot showing the significant partial (Spearman) correlation between PFAS and the metabolites, lipids, and compound class of the cell media extract ion of HepaRG cells exposed to PFAS. Intra-metabolites, lipids, and compound class correlations have been removed for clarity. The orange color indicates a positive correlation, and the green color represents a negative correlation. **Abbreviation:** Phosphatidylcholines (PC), Cholesteryl esters (CE), Phosphatidylethanolamines (PE), Sphingomyelins (SM), Triacylglycerides (TG), Phosphatidylinositol (PI), Phosphatidylserine (PS), Acyl Carnitines (AC), Carnitines (CAR), AC/CAR (Acyl Carnitines / Carnitines ratio), Lysophosphatidylcholine (LPC), Nucleotides (NT), Peptides (PEP), Phosphocholines (Cho), Vitamin derivatives (Vder), 5-Aminoimidazole-4-carboxamide ribonucleotide (AICAR), Carboxylic acids (CA), Hydroxy fatty acids (OH-FA), Amino acids (AA). (For interpretation of the references to colour in this figure legend, the reader is referred to the web version of this article.)

correlations with bile acids and the steroid class. PFOS also demonstrated a positive correlation with the bile acid pool level in the extracellular media (Fig. 4E). The metabolic signature of PFAS exposure in the steatosis model is in the chord plot in Fig. 4F, indicating an interplay between the PFAS and several polar and semipolar metabolites, including various carbohydrates, amino acid derivatives, nucleosides, and nucleotide-related metabolites, as well as several bile acids, such as GCDCA, GHCA, TCDCA, TDCA, and TLCA.

3.4. Pathway patterns in hepatocytes under steatosis and PFAS exposure reveal multiple mitochondrial disruptions

Pathway analysis was performed in MetaboAnalyst 6.0 with the aim of identifying key metabolic pathways affected by PFAS exposure, steatosis, and their combined effects. Overall, the pathway analyses showed that 30 metabolic pathways were affected by the exposures, involving lipid metabolism, amino acid-related pathways, steroid synthesis, and carbohydrate metabolism, all of which are directly or indirectly connected to the mitochondria or mitochondria-associated membranes (Fig. 5). Table S5 shows all detected pathways identified in each comparison.

The HepaRG cell steatosis model exposed to PFAS was characterized by six distinct significant pathways (Fig. 5), related to the amino acid metabolism (glutamate, glycine, serine, alanine, threonine, and histidine metabolism), central energy metabolism that reflect changes in the flux of TCA cycle (pyruvate and propanoate metabolism), as well as the one-carbon metabolism (folate cycle metabolism). In the context of HepaRG cells exposed to the PFAS mixture (without steatosis), the most significantly enriched impact pathways in this model were selenoamino acid metabolism, *de novo* fatty acid and steroid biosynthesis, vitamin and cofactor (B1, E, H) metabolism, and xenobiotic metabolism. On the other hand, the HepaRG steatosis model showed that, in this context, the uniquely altered pathways were glycerophospholipid and vitamin D3 signaling metabolism. Interestingly, the pathways that represent the critical nodes across all scenarios (steatosis, PFAS exposure, and their combination) are linked to inflammation and lipid homeostasis: leukotriene metabolism and squalene and cholesterol biosynthesis.

3.5. Distinct and combined effects of PFAS and steatosis on hepatocyte mitochondrial respiration

To further understand how PFAS exposure, steatosis, and their interplay affect mitochondrial function, we performed a Seahorse XF Cell Mito Stress Test to evaluate key parameters of mitochondrial respiration and bioenergetic capacity in HepaRG cells (Fig. 6). Basal respiration, measuring the oxygen consumption required to sustain routine mitochondrial activity, was significantly elevated in OAPA-treated (Oleic acid, Palmitic acid: MASLD-like steatosis) HepaRG cells compared to PFAS-treated cells, with OAPA + PFAS showing significantly lower basal respiration than the OAPA exposure. Maximal respiration, reflecting the upper limit of mitochondrial respiratory capacity, was significantly reduced in the PFAS and OAPA + PFAS groups compared with the OAPA-exposed cells. Proton leak, assessing non-ATP-linked oxygen consumption, was significantly elevated under OAPA exposure compared with the PFAS-exposed groups. ATP production, quantifying respiration linked to ATP synthesis, increased significantly under OAPA exposure but markedly decreased in the PFAS-exposed cells. Coupling efficiency, defined as the proportion of respiration dedicated to ATP generation, was significantly higher in the OAPA and OAPA + PFAS-exposed groups than in controls and was highest in the OAPA + PFAS group, which also exceeded the PFAS-alone group. Spare respiratory capacity, reflecting the ability of mitochondria to respond to increased energetic demand, was detectable and comparable between controls and PFAS-exposed cells, but was markedly reduced in both OAPA- and OAPA + PFAS-exposed cells. Non-mitochondrial respiration, representing oxygen consumption independent of mitochondrial activity, was likewise elevated with OAPA but declined upon PFAS and OAPA + PFAS exposure.

We next examined whether the lipid-based compositional fractions were associated with mitochondrial functional state. Spearman correlation analysis showed that, in the OAPA condition, cardiolipin abundance and the Mito-like fraction were significantly associated with multiple mitochondrial respiratory parameters. Notably, in the combined PFAS + OAPA condition, both the Mito-like and LD-like fractions were significantly associated with several mitochondrial respiration measurements, including basal respiration, maximal respiration, proton leak, ATP production, coupling efficiency, and spare respiratory capacity (Fig. 7). These findings collectively indicate that treatment-dependent changes in the mitochondria-enriched fraction are biologically linked to mitochondrial functional state, particularly under conditions exhibiting the most pronounced combined phenotype.

4. Discussion

In this study, we conducted comprehensive metabolomics and lipidomics analysis of mitochondria-enriched hepatocyte fractions and extracellular media to investigate how PFAS exposure affects mitochondrial metabolism under steatotic and non-steatotic conditions. Our findings, therefore, reflect acute metabolic perturbations (24 h of exposure) rather than chronic, cumulative effects of long-term PFAS exposure. We identified both shared and condition-specific metabolic dysregulation patterns relative to non-exposed HepaRG controls, revealing common effects of PFAS exposure and steatosis on metabolic pathways as well as a distinct PFAS-induced mitochondrial fingerprint in hepatocytes. In addition to global effects of the PFAS mixture on the mitochondrial environment, we observed significant associations between individual PFAS and specific metabolites as well as metabolite classes, underscoring the importance of accounting for PFAS-specific phenotypic responses in metabolic regulation.

At the metabolite class level, a distinct metabolic pattern was observed in the mitochondria-enriched fraction of steatosis-exposed and steatosis-PFAS-exposed HepaRG cells, characterized by increased levels

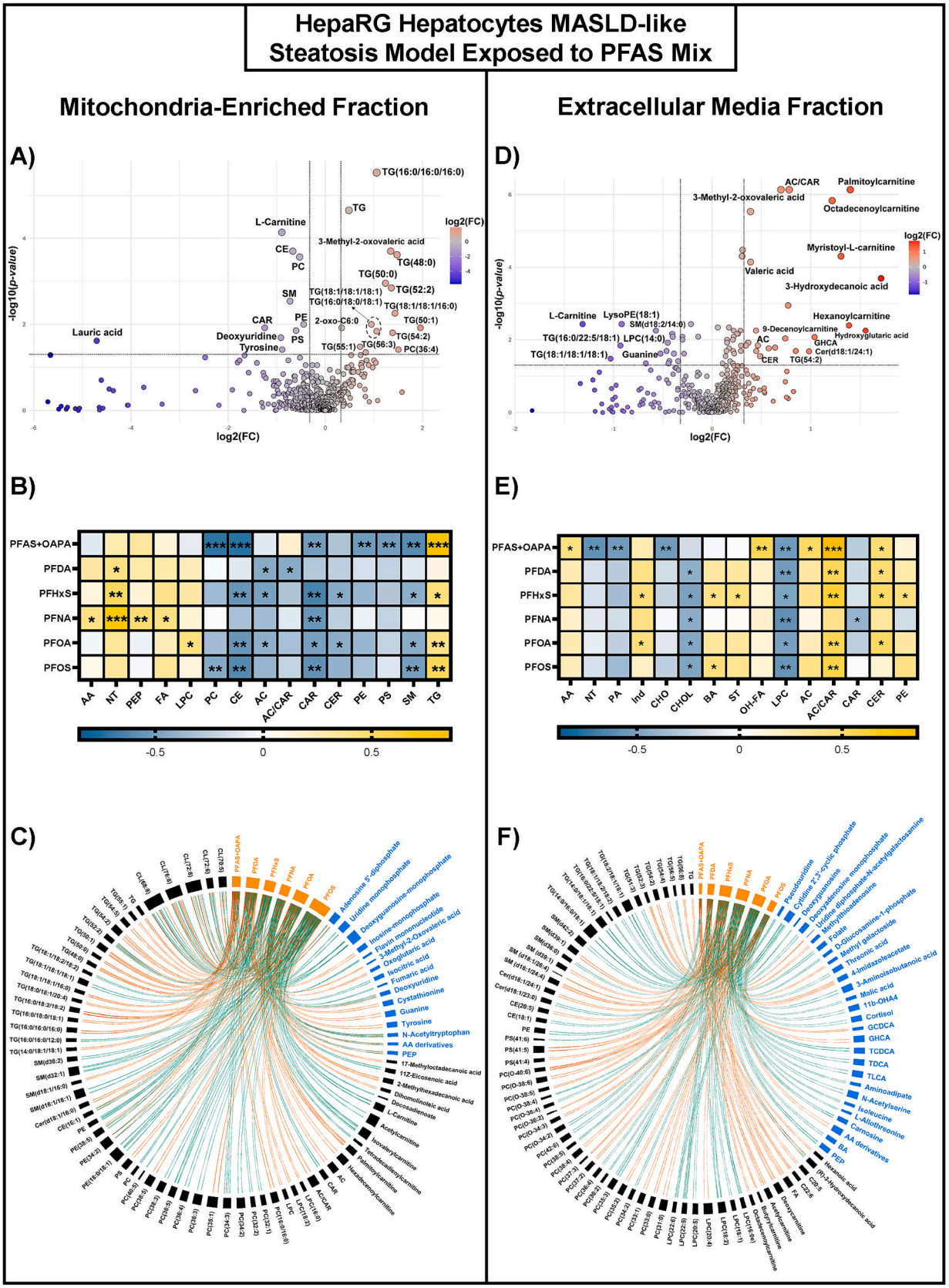

(caption on next page)

Fig. 4. Metabolic impact of PFAS exposure under steatotic conditions. A) Volcano plot showing the significantly altered metabolites, lipids, and compound classes (FC>±1.25, $p < 0.05$) between the mitochondrial-enriched fraction of the HepaRG steatosis cell model exposed to the PFAS mix model and the control HepaRG model. **B)** Heatmap showing the significant ($p < 0.05$) metabolic patterns between the two mitochondrial-enriched fractions (steatosis-PFAS-exposed x control). **C)** Chord plot showing the significant partial (Spearman) correlation between PFAS and the metabolites, lipids, and compound class of the mitochondrial-enriched fraction of HepaRG steatosis cells exposed to PFAS. Intra-metabolites, lipids, and compound class correlations have been removed for clarity. The orange color indicates a positive correlation, and the green color represents a negative correlation. **D)** Volcano plot showing the significantly altered metabolites, lipids, and compound classes (FC>±1.25, p < 0.05) between the cell media extract of HepaRG steatosis cells exposed to the PFAS mix model and the control HepaRG model. **E)** Heatmap showing the significant ($p < 0.05$) metabolic patterns between the two cell media extracts (steatosis-PFAS-exposed control). **F)** Chord plot showing the significant partial (Spearman) correlation between PFAS and the metabolites, lipids, and compound class of the cell media extract ion of HepaRG steatosis cells exposed to PFAS. Intra-metabolites, lipids, and compound class correlations have been removed for clarity. The orange color indicates a positive correlation, and the green color represents a negative correlation. **Abbreviation**: OAPA (Oleic acid, Palmitic acid: steatosis), Phosphatidylcholines (PC), Cholesteryl esters (CE), Phosphatidylethanolamines (PE), Sphingomyelins (SM), Triacylglycerides (TG), Phosphatidylinositol (PI), Phosphatidylserine (PS), Acyl Carnitines (AC), Carnitines (CAR), AC/CAR (Acyl Carnitines / Carnitines ratio), lysophosphatidylcholine (LPC), Nucleotides (NT), Peptides (PEP), Bile acids (BA), Steroids and derivates (ST), Phosphocholines (CHOL), Polyamines (PA), Indoles (Ind), Carbohydrates (CHO), Carboxylic acids (CA), Hydroxy fatty acids (OH-FA), Amino acids (AA). (For interpretation of the references to colour in this figure legend, the reader is referred to the web version of this article.)

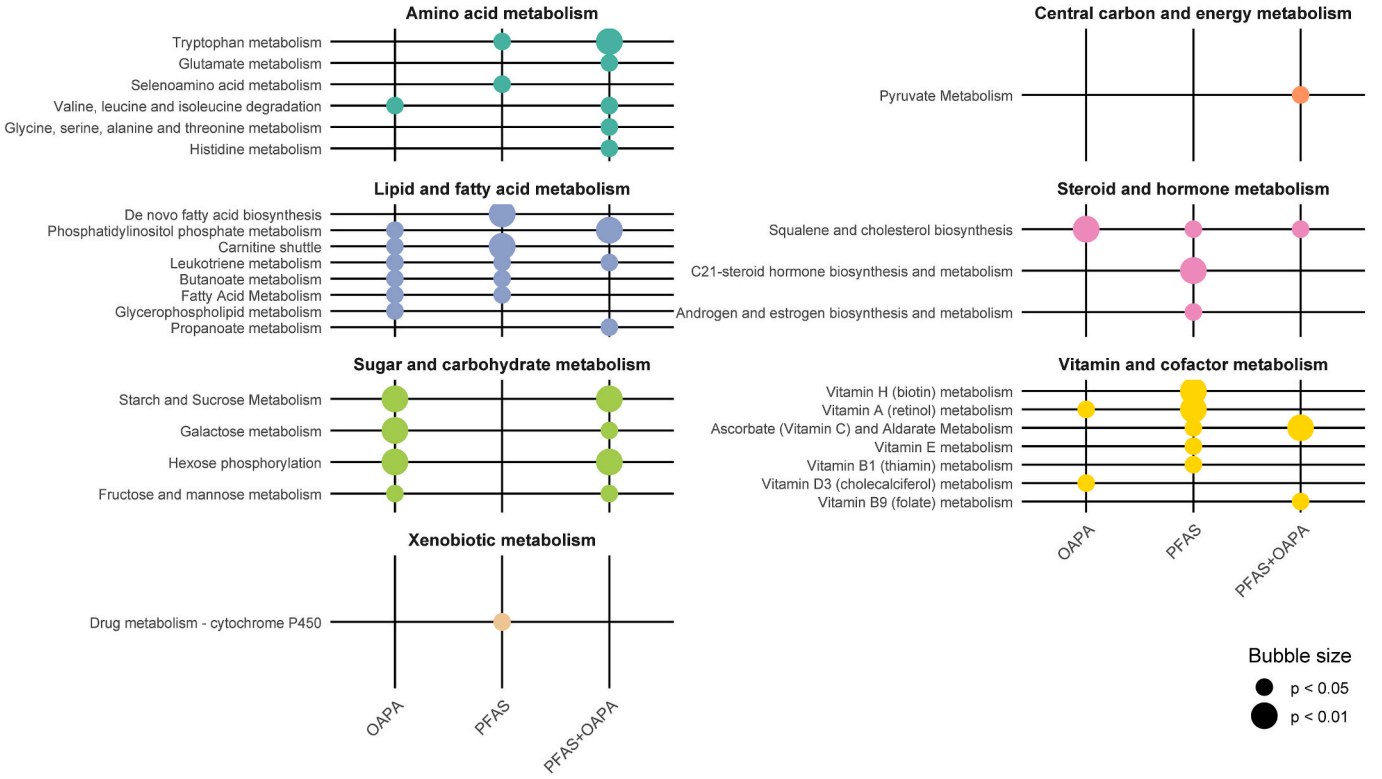

Fig. 5. Pathway analysis of mitochondrial-enriched fractions from HepaRG cells under steatosis (OAPA), PFAS exposure, and combined steatosis–PFAS conditions. The size of the bubble represents the *p*-value level of significance. **Abbreviation:** OAPA (Oleic acid, Palmitic acid), PFAS (per- and polyfluoroalkyl substances).

of several TG lipids compared to non-exposed HepaRG cells. The presence of TGs in an enriched mitochondrial extract during lipid excess, such as in steatosis, might support the growing evidence of the association between mitochondria and lipid droplets (LDs) and the formation of peridroplet mitochondria (PDM), not only through physical contact but also as a metabolic axis connecting mitochondria to LDs (Talari, 2023; Fan et al., 2024; Benador, 2018; Su et al., 2023; Aon et al., 2014). The LDs are a highly dynamic storage pool of fatty acids in the form of TG species, and their excessive accumulation is one of the hallmarks of steatosis (Su et al., 2023; Aon et al., 2014). Previous studies have indicated that the PDM may act as an adaptive response under physiological conditions that require LD expansion, which is initiated by activating ATP-demanding functions such as acyl-CoA synthesis, lipid cycling, and increased TCA cycle activity to produce citrate for *de novo* lipogenesis (Benador, 2018; Prentki and Madiraju, 2012).

The combined steatosis-inducing fatty-acid and PFAS exposure elicited a substantially pronounced downregulation of lipids across multiple lipid classes (PC, PE, SM, CE), revealing a stronger combined effect that surpassed the impact of each exposure alone. These lipids are central mitochondrial components or act as modulators of membrane fluidity and signaling molecules. These findings align with previous studies showing altered mitochondrial membrane integrity and changes in membrane fluidity, both in the hepatocyte steatosis model (Zhang et al., 2011), as well as in hepatocytes exposed to PFAS (Alijagic, 2024; Xiaopeng and Jin, 2023). Although previous findings revealed the impact of PFAS exposure on the mitochondrial membrane, our study indicates potential PFAS-associated changes in cardiolipins within the mitochondria-enriched fraction. Cardiolipins are exclusively mitochondrial phospholipids localized to the inner mitochondrial membrane and play a key role in maintaining mitochondrial stability, membrane structure, and other essential functions, thereby ensuring mitochondrial homeostasis (Paradies et al., 2019). This phospholipid class is particularly susceptible to increased oxidative stress, and its peroxidation has been linked to mitochondrial dysfunction in MASLD by disrupting the

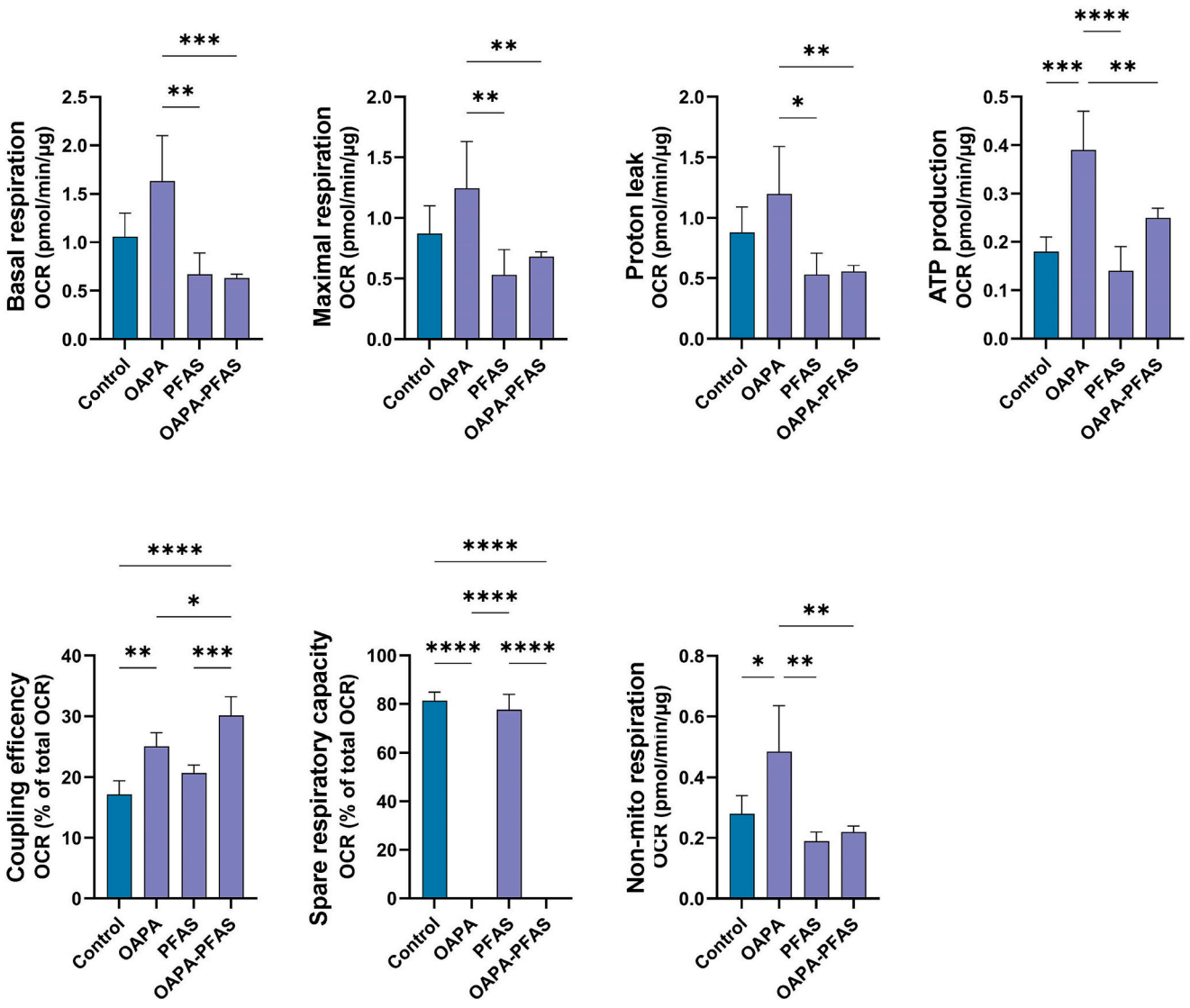

Fig. 6. Mitochondrial respiration profiles of HepaRG cells under control, OAPA-induced steatosis, PFAS exposure, and combined OAPA + PFAS exposure. Basal respiration, ATP-linked respiration, proton leak, maximal respiration, spare respiratory capacity, coupling efficiency, and non-mitochondrial respiration were quantified using the Agilent Seahorse XFp Cell Mito Stress Test. Data are presented as mean ± SD (n = 3). Statistical significance was assessed by one-way ANOVA followed by Tukey's post hoc test. Level of significance: $*p < 0.05$, $**p < 0.01$, $***p < 0.001$, $****p < 0.0001$. **Abbreviation:** OAPA (Oleic acid, Palmitic acid), PFAS (per- and polyfluoroalkyl substances).

electron transport chain, altering mitochondrial permeability, and mediating the release of cytochrome *c* from mitochondria (Paradies et al., 2014). Due to reported PFAS-induced high levels of mitochondrial ROS in hepatocytes caused by calcium overload (Alijagic, 2024), and considering the essential role of cardiolipins in mitochondrial function, this phospholipid has been hypothesized as a relevant mitochondrial biomarker for environmental exposure (Reddam et al., 2022). Our data indicate that PFAS-associated cardiolipin changes are more pronounced in the steatotic HepaRG model, consistent with greater alteration of cardiolipin-containing lipid composition within the mitochondria-enriched fraction during fatty acid overload.

We also observed a high level of ACs and a strong upregulation of the AC/CAR ratio in the extracellular media of the HepaRG steatosis model and in the steatosis-PFAS-exposed HepaRG. Long-chain fatty acids rely on esterification with L-carnitine to form acetyl-L-carnitine, enabling their transport from the cytoplasm to the mitochondrial matrix for energy production through mitochondrial β-oxidation (Savic et al. , 2020). Dysregulation of this carnitine shuttle has been identified as one of the key features of liver disease and is also impacted by PFAS exposure (Peng, 2013; Savic et al., 2020). Short- and long-chain ACs have been identified as potential biomarkers of PFAS exposure and also as predictors of disease severity in patients with liver disease (Peng, 2013; Enooku, 2019). L-Carnitine was consistently reduced in the mitochondria-enriched fraction of the steatosis model (exposed and non-exposed to PFAS), while increased levels of short, medium, and long-chain ACs were observed in the media. This pattern may reflect impaired fatty acid handling and altered carnitine shuttle activity under PFAS exposure, especially in the context of steatosis. Under these conditions, excess fatty acids may compete for limited carnitine, leading to incomplete mitochondrial β-oxidation (Savic et al., 2020; Roth, 2021). Increased extracellular ACs may therefore reflect altered metabolic handling under stress, although passive release secondary to cell stress cannot be fully excluded.

In addition to lipid-related alterations, our data indicate that PFAS exposure perturbs multiple interconnected metabolic processes linked to mitochondrial function, including fatty acid handling, peptide turnover, amino acid metabolism, nucleotide balance, and bile acid-related responses. Notably, lauric acid, which was decreased in the mitochondria-

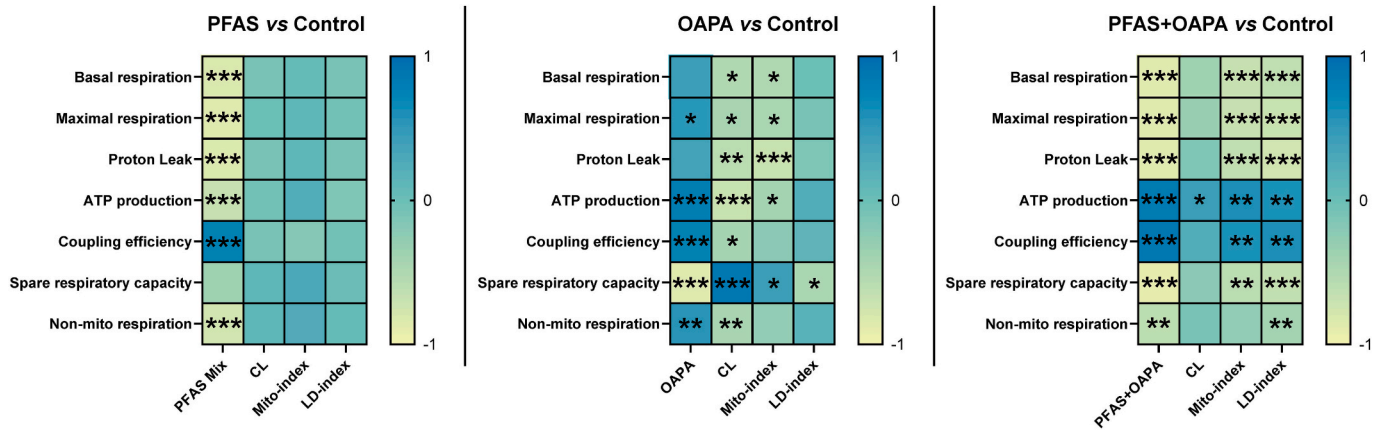

Fig. 7. Spearman correlation analyses between cardiolipin abundance (CL), the Mito-like fraction (Mito-index), the LD-like fraction (LD-index), and Seahorse respiratory parameters (Basal and Maximal respiration, Proton leak, ATP production, Coupling efficiency, Spare respiratory condition, and Non-mito respiration) in the steatosis (OAPA), PFAS, and PFAS + OAPA conditions, respectively. Significant correlations were defined as $^{*}p < 0.05$, $^{**}p < 0.01$, $^{***}p < 0.001$. These analyses were used to assess whether treatment-dependent remodeling of the mitochondria-enriched fraction was associated with mitochondrial functional state. Exposure conditions: PFAS mix (containing 47.8% PFOS, 28.7% PFOA, 12.1% PFHxS, 6.3% PFDA, and 5.1% PFNA, in a total concentration of 22.44 μmol L^{-1}); OAPA (Oleic acid, Palmitic acid: steatosis-induced treatment); PFAS + OAPA (combination exposure of the PFAS mix + OAPA-induced steatosis).

enriched fraction of PFAS-exposed steatotic HepaRG cells, has been proposed as a promising candidate for MASLD treatment, as its administration has been shown to improve serum TG levels, blood glucose, and insulin sensitivity, and to reduce hepatic apoptosis through decreased annexin V expression (Sedik, 2024). Furthermore, in addition to the lipid-related effects in the mitochondrial environment, we also observed several polar and semipolar metabolites, as well as their respective metabolite classes, playing a key role in mitochondrial dysfunction, especially in the presence of PFAS exposure. For instance, we observed an increased level of peptides in the mitochondria-enriched fraction of PFAS-exposed HepaRG cells (Fig. 3). Elevated peptides in the mitochondria-rich fraction may indicate changes in protein turnover or stress-induced metabolic remodeling (Merry, 2020). The positive correlation between PFNA and amino acids, as well as nucleotides in PFAS-exposed HepaRG cell models under both steatotic and non-steatotic conditions, suggests interference with amino acid and nucleotide metabolism. Additionally, the buildup of nucleotides might be a response to cellular stress (India-Aldana, 2023; Addicks, 2025), although the current data do not pinpoint the exact upstream mechanism. Moreover, analysis of the extracellular media from PFAS-exposed HepaRG cells revealed increased abundance of specific metabolites, including bile acids, suggesting a hepatoprotective response to PFAS exposure, consistent with previous reports (Alijagic, 2024).

A decreased level of the branched-chain keto acid (BCKA), 3-methyl-2-oxovaleric acid, was observed in the mitochondria-enriched fraction of steatotic hepatocytes. This reduction likely reflects impaired mitochondrial metabolic flux associated with steatosis, leading to inefficient oxidation and consequent intracellular accumulation of BCKA (Nishi, 2023; Walejko, 2021). To mitigate BCKA-associated toxicity, these metabolites may accumulate in the extracellular media, consistent with elevated extracellular levels of 3-methyl-2-oxovaleric acid observed in the steatosis model. In contrast to steatosis alone, which reduced mitochondrial levels of 3-methyl-2-oxovaleric acid, combined PFAS exposure and steatosis resulted in increased mitochondrial accumulation of this BCKA, accompanied by a similar accumulation in the extracellular media. This pattern suggests that PFAS exacerbates mitochondrial dysfunction by promoting mitochondrial accumulation of BCKA despite the impaired oxidative capacity associated with steatosis. These findings support the hypothesis that mitochondrial disruption can override PPAR-mediated BCKA catabolism, leading to pathological BCKA accumulation. (Gebreab, 2020).

Our data reveals a broad cascade of PFAS-induced mitochondrial effects spanning lipid and central metabolism, collectively disrupting key mitochondrial energy pathways. Functional pathway analysis indicated that PFAS exposure in non-steatotic HepaRG cells elicits adaptive stress responses, primarily through increased selenoprotein activity and selenoamino acid metabolism, likely reflecting altered oxidative stress and redox balance (Zhang, et al., 2020). In addition, perturbations in vitamin metabolism (B1, E, biotin/H) point to disrupted energy and redox homeostasis, as these vitamins serve as cofactors for mitochondrial and membrane-associated redox enzymes (Nguyen et al., 2024; Liu, et al., 2025). Furthermore, PFAS-induced alterations in *de novo* fatty acid synthesis and steroid/hormone biosynthesis pathways are consistent with previous reports demonstrating disruption of lipid-metabolizing genes (*e.g.*, *SREBP1*, *FASN*, *ACC*) and nuclear hormone receptor signaling, including PPARs, thereby modulating hepatic lipid synthesis and hormone-related gene expression even in the absence of established steatosis (Qi, 2023; Charni-Natan et al., 2019).

Under conditions of combined steatosis and PFAS exposure, we identified a distinct set of metabolic disruptions primarily affecting mitochondrial-associated amino acids, mitochondrial flux through the TCA cycle, and folate metabolism. These findings align with previous reports showing that amino acid–related pathways are perturbed by PFAS exposure and steatosis individually (Guo, 2022; Maltais-Payette, 2025), supporting a greater perturbation effect of their combination in mediating metabolic stress and adaptive responses in hepatocytes. Notably, folate metabolism has emerged as a potential therapeutic target to prevent dyslipidemia and mitigate adverse health effects associated with PFAS exposure (Zhang, 2023).

In the HepaRG steatosis model, functional pathway analysis further highlighted glycerophospholipid and vitamin D3 metabolism as significantly altered pathways. Both are well-established features of steatosis-associated lipid dysregulation, with roles in membrane integrity, signaling, and LD formation, and vitamin D-mediated modulation of insulin resistance (Brown et al., 2013; Lee et al., 2024). Across steatosis, PFAS exposure, and their combination, leukotriene metabolism and squalene and cholesterol biosynthesis emerged as common perturbed pathways. Leukotriene metabolism, which involves arachidonic acid–derived lipid mediators central to inflammation and immune responses, is known to be influenced by PFAS exposure and linked to liver injury and inflammation under both steatotic and non-steatotic conditions (Yu, 2016). In parallel, both steatosis and PFAS exposure have been shown to impair squalene and cholesterol biosynthesis by disrupting hepatic lipid and sterol metabolism (Vujic et al., 2024; Liu, 2021). Taken together, these findings identify convergent nodes of lipid metabolism and inflammation that respond to steatosis and PFAS exposure, either

independently or in combination.

The Seahorse mitochondrial stress analysis supported these molecular findings by demonstrating distinct bioenergetic alterations under steatosis, PFAS exposure, and their combination. Steatosis increased basal and maximal respiration, consistent with elevated lipid oxidation and ATP demand, but nearly abolished spare respiratory capacity, indicating that mitochondria operate close to their functional limit under lipid overload. In contrast, PFAS exposure reduced basal and maximal respiration, reflecting impaired mitochondrial function and diminished oxidative capacity. Notably, combined steatosis and PFAS exposure reproduced the PFAS-induced suppression of respiration while preserving the steatosis-associated loss of respiratory reserve, suggesting that steatosis further aggravates the bioenergetic vulnerability to PFAS. These functional impairments align with the observed lipid remodeling and cardiolipin disruption, highlighting mitochondrial respiratory dysfunction as a convergent mechanism in the PFAS-steatosis axis.

Several limitations of the study should be acknowledged. While our findings support the growing evidence for the mitochondrial-LD axis and PDM formation, we did not quantify PDM formation. In addition, the use of differential centrifugation to isolate mitochondria-enriched fractions under steatotic conditions may result in partial co-isolation of LD-associated endoplasmic reticulum, mitochondrial-associated membranes, or cytosolic components, as previously reported (Talari, 2023; Benador, 2018; Veliova et al., 2020). In addition, both steatosis and PFAS exposure may alter mitochondrial abundance within the enriched fraction. To mitigate these effects, metabolite levels were normalized to protein content, complemented by internal standards, pooled QC controls, and per-total-cell normalization for PFAS concentration. To enhance interpretation, we included lipid-based compositional fractions derived from LC-HRMS lipidomics data. These fractions revealed a dominant mitochondrial signature linked to cardiolipin levels across all groups, a consistently low ER/MAM-like fraction, and increased TG-related remodeling in steatotic conditions, with the strongest functional links in the PFAS-steatosis group. However, because these fractions are indirect lipid-class-based indicators, the results should be interpreted as reflecting changes in a mitochondria-enriched fraction with exposure-dependent compositional shifts, rather than as conclusive evidence of per-mitochondrion remodeling. Nevertheless, future studies incorporating orthogonal mitochondrial metrics such as citrate synthase activity, mtDNA copy number, and protein markers including VDAC and TOMM20, together with markers of potential contaminants, would further validate the extent of PFAS-steatosis-associated remodeling at the per-mitochondrion level beyond the mitochondria-enriched fraction analyzed in this study. This study used co-exposure to PFAS and palmitate/oleate to simulate acute metabolic disruptions during fatty acid overload. Future data comparing simultaneous and sequential exposure will be valuable for validating the PFAS-steatosis mechanistic axis by clarifying how existing steatosis or prior PFAS exposure uniquely affects mitochondrial responses. Moreover, given the non-monotonic dose–response behavior of PFAS in cellular phenotypic and metabolic outcomes (Alijagic, 2024), alternative PFAS concentrations may elicit distinct metabolic responses as the ones observed here.

In summary, this study demonstrates that PFAS exposure perturbs the mitochondrial environment in hepatocytes and exacerbates metabolic dysfunction under steatotic conditions. We identify a distinct metabolic fingerprint associated with steatosis, PFAS exposure, and their combination, converging on the mitochondrial-LD axis and characterized by impaired mitochondrial phospholipid composition alongside increased TGs indicative of LD formation. PFAS-induced remodeling of cardiolipin within mitochondria-enriched fractions further suggests disruption of the mitochondrial inner membrane. Additionally, increased extracellular abundance of ACs, most notably palmitoylcarnitine, points to impaired mitochondrial β-oxidation, likely reflecting disrupted fatty acid activation and transport into mitochondria. Perturbations in amino acids, nucleotides, and peptides further indicate PFAS-driven disruption of central carbon metabolism and activation of DNA/RNA repair pathways, consistent with increased oxidative stress in the mitochondrial environment. Collectively, our findings highlight inflammatory, immune, and lipid-homeostasis pathways as key targets of PFAS and steatosis, suggesting that mitochondrial-focused interventions may offer therapeutic potential to mitigate the metabolic burden associated with PFAS exposure.

CRediT authorship contribution statement

João Marcos G. Barbosa: Writing – review & editing, Writing – original draft, Visualization, Validation, Supervision, Software, Methodology, Investigation, Formal analysis, Data curation, Conceptualization. **Andi Alijagic:** Writing – review & editing, Writing – original draft, Visualization, Validation, Software, Resources, Methodology, Investigation, Formal analysis, Data curation, Conceptualization. **Anh Hoang Nguyen:** Writing – review & editing, Methodology, Formal analysis, Data curation. **Victor Castro-Alves:** Writing – review & editing, Methodology, Formal analysis, Data curation. **Lorane Valgueblasse:** Writing – review & editing, Methodology, Formal analysis. **Matej Orešič:** Writing – review & editing, Resources, Project administration, Funding acquisition, Conceptualization. **Tuulia Hyötyläinen:** Writing – review & editing, Writing – original draft, Visualization, Validation, Supervision, Software, Resources, Project administration, Methodology, Investigation, Funding acquisition, Formal analysis, Data curation, Conceptualization.

Declaration of competing interest

The authors declare that they have no known competing financial interests or personal relationships that could have appeared to influence the work reported in this paper.

Acknowledgements

We thank Emma Bergman and Rongrong Wu for their help with the Seahorse assay analysis.

This study was supported by the Swedish Research Council (grant no. 2020-03674 to T.H and M.O.), Formas (grant no. 2019-00869 to T.H and M.O.), Novo Nordisk Foundation (grant no. NNF21OC0070309 to T.H.), by the “Investigation of endocrine-disrupting chemicals as contributors to progression of metabolic dysfunction-associated steatotic liver disease” (EDC-MASLD) consortium funded by the Horizon Europe Program of the European Union under Grant Agreement 101136259 (to T.H. and M.O.), and by the Swedish Knowledge Foundation (grant no. 20220122, to T.H. and M.O.). Views and opinions expressed are those of the author (s) only and do not necessarily reflect those of the European Union. Neither the European Union nor the granting authority can be held responsible for them.

Appendix A. Supplementary data

Supplementary data to this article can be found online at https://doi.org/10.1016/j.envint.2026.110337. Supplementary data 1 contains Figs. S1-S4. Supplementary data 2 contains Tables S1-S5.

Data availability

Metabolomics MS-based data are deposited in the MassIVE repository (https://massive.ucsd.edu/) under the code: MSV000100524.

References

Brusseau, M.L., Anderson, R.H., Guo, B., 2020. PFAS concentrations in soils: background levels versus contaminated sites. Sci. Total Environ. 740, 140017.

Kurwadkar, S., et al., 2022. Per- and polyfluoroalkyl substances in water and wastewater: a critical review of their global occurrence and distribution. Sci. Total Environ. 809, 151003.

Morales-McDevitt, M.E., et al., 2021. The air that we breathe: neutral and volatile PFAS in indoor air. Environ. Sci. Technol. Lett. 8, 897–902.
Li, J., Sun, J., Li, P., 2022. Exposure routes, bioaccumulation and toxic effects of per- and polyfluoroalkyl substances (PFASs) on plants: a critical review. Environ. Int. 158, 106891.
Soerensen, A.L., Benskin, J.P., Faxneld, S., 2024. Four decades of spatiotemporal variability of per- and polyfluoroalkyl substances (PFASs) in the baltic sea. Environ. Sci. Technol. 58, 10806–10816.
De Silva, A.O., et al., 2021. PFAS Exposure Pathways for Humans and Wildlife: a Synthesis of Current Knowledge and Key Gaps In Understanding. Environ. Toxicol. Chem. 40, 631–657.
Salihovic, S., et al., 2018. Changes in markers of liver function in relation to changes in perfluoroalkyl substances - a longitudinal study. Environ. Int. 117, 196–203.
Momo, H.D., Alvarez, C.S., Purdue, M.P., Graubard, B.I., McGlynn, K.A., 2024. Associations of per- and polyfluoroalkyl substances and nonalcoholic fatty liver disease in the United States adult population, 2003-2018. Environ. Epidemiol. (Philadelphia, Pa.) 8, e284.
Zhang, J., et al., 2024. Association between serum per- and polyfluoroalkyl substances levels and metabolic dysfunction-associated steatotic liver disease. Environ. Pollut. 363, 125233.
Alijagic, A., et al., 2024. Metabolic and phenotypic changes induced by PFAS exposure in two human hepatocyte cell models. Environ. Int. 190.
Evans, N., et al., 2022. In vitro activity of a panel of per- and polyfluoroalkyl substances (PFAS), fatty acids, and pharmaceuticals in peroxisome proliferator-activated receptor (PPAR) alpha, PPAR gamma, and estrogen receptor assays. Toxicol. Appl. Pharmacol. 449, 116136.
Yang, W., et al., 2023. PPARα/ACOX1 as a novel target for hepatic lipid metabolism disorders induced by per- and polyfluoroalkyl substances: an integrated approach. Environ. Int. 178, 108138.
Liu, Y., et al., 2023. Mitochondrial dysfunction in metabolic disorders induced by per- and polyfluoroalkyl substance mixtures in zebrafish larvae. Environ. Int. 176, 107977.
Peng, S., et al., 2013. An integrated metabonomics and transcriptomics approach to understanding metabolic pathway disturbance induced by perfluorooctanoic acid. J. Pharm. Biomed. Anal. 86, 56–64.
Huang, Q., et al., 2013. Perfluorooctanoic acid induces apoptosis through the p53-dependent mitochondrial pathway in human hepatic cells: a proteomic study. Toxicol. Lett. 223, 211–220.
Li, K., Geng, Y., Lin, B., Xi, Z., 2023. Molecular mechanisms underlying mitochondrial damage, endoplasmic reticulum stress, and oxidative stress induced by environmental pollutants. Toxicol. Res. (camb) 12, 1014–1023.
Reddam, A., McLarnan, S., Kupsco, A., 2022. Environmental chemical exposures and mitochondrial dysfunction: a review of recent literature. Curr. Environ. Heal. Reports 9, 631–649.
Naviaux, R.K., 2020. Perspective: cell danger response Biology-the new science that connects environmental health with mitochondria and the rising tide of chronic illness. Mitochondrion 51, 40–45.
Suzuki, T., Hidaka, T., Kumagai, Y., Yamamoto, M., 2020. Environmental pollutants and the immune response. Nat. Immunol. 21, 1486–1495.
Meyer, J.N., et al., 2013. Mitochondria as a target of environmental toxicants. Toxicol. Sci. 134, 1–17.
Roubicek, D.A., de Souza-Pinto, N.C., 2017. Mitochondria and mitochondrial DNA as relevant targets for environmental contaminants. Toxicology 391, 100–108.
Louisse, J., et al., 2023. Determination of in vitro hepatotoxic potencies of a series of perfluoroalkyl substances (PFASs) based on gene expression changes in HepaRG liver cells. Arch. Toxicol. 97, 1113–1131.
Gómez-Lechón, M.J., et al., 2007. A human hepatocellular in vitro model to investigate steatosis. Chem. Biol. Interact. 165, 106–116.
Penke, M., et al., 2017. Oleate ameliorates palmitate-induced reduction of NAMPT activity and NAD levels in primary human hepatocytes and hepatocarcinoma cells. Lipids Health Dis. 16, 191.
Campos-Espinosa, A., Guzmán, C., 2021. A model of experimental steatosis in vitro: hepatocyte cell culture in lipid overload-conditioned medium. J. Vis. Exp. https://doi.org/10.3791/62543.
Rose, S., et al., 2022. DMSO-free highly differentiated HepaRG spheroids for chronic toxicity, liver functions and genotoxicity studies. Arch. Toxicol. 96, 243–258.
Dei Cas, M., et al., 2020. A straightforward LC-MS/MS analysis to study serum profile of short and medium chain fatty acids. J. Chromatogr. B 1154, 121982.
Schmid, R., et al., 2023. Integrative analysis of multimodal mass spectrometry data in MZmine 3. Nat. Biotechnol. 41, 447–449.
Salek, R.M., Steinbeck, C., Viant, M.R., Goodacre, R., Dunn, W.B., 2013. The role of reporting standards for metabolite annotation and identification in metabolomic studies. GigaScience 2, 1.
Pang, Z., et al., 2024. MetaboAnalyst 6.0: towards a unified platform for metabolomics data processing, analysis and interpretation. Nucleic Acids Res. 52, W398–W406.
Wishart, D.S., et al., 2022. HMDB 5.0: the human metabolome database for 2022. Nucleic Acids Res. 50, D622–D631.
Conroy, M.J., et al., 2024. LIPID MAPS: update to databases and tools for the lipidomics community. Nucleic Acids Res. 52, D1677–D1682.
Lu, Y., Pang, Z., Xia, J., 2023. Comprehensive investigation of pathway enrichment methods for functional interpretation of LC–MS global metabolomics data. Brief. Bioinform. 24, bbac553.
Kanehisa, M., Sato, Y., Furumichi, M., Morishima, K., Tanabe, M., 2019. New approach for understanding genome variations in KEGG. Nucleic Acids Res. 47, D590–D595.
Talari, N.K., et al., 2023. Lipid-droplet associated mitochondria promote fatty-acid oxidation through a distinct bioenergetic pattern in male Wistar rats. Nat. Commun. 14, 766.
Fan, H. & Tan, Y. Lipid Droplet–Mitochondria Contacts in Health and Disease. International Journal of Molecular Sciences vol. 25 at Doi: 10.3390/ijms25136878 (2024).
Benador, I.Y., et al., 2018. Mitochondria bound to lipid droplets have unique bioenergetics, composition, and dynamics that support lipid droplet expansion. Cell Metab. 27, 869–885.e6.
Su, W., Chi, Y., An, Y.A., 2023. Editorial: Lipid droplets and mitochondria in metabolic diseases. Front. Physiol. 14.
Aon, M.A., Bhatt, N., Cortassa, S.C., 2014. Mitochondrial and cellular mechanisms for managing lipid excess. Front. Physiol. Volume 5-.
Prentki, M., Madiraju, S.R.M., 2012. Glycerolipid/free fatty acid cycle and islet β-cell function in health, obesity and diabetes. Mol. Cell. Endocrinol. 353, 88–100.
Zhang, Y., Jiang, L., Hu, W., Zheng, Q., Xiang, W., 2011. Mitochondrial dysfunction during in vitro hepatocyte steatosis is reversed by omega-3 fatty acid–induced up-regulation of mitofusin 2. Metabolism 60, 767–775.
Xiaopeng, C., Jin, T., 2023. Perfluorooctane sulfonate (PFOS) causes aging damage in the liver through the mt-DNA-mediated NLRP3 signaling pathway. Ecotoxicol. Environ. Saf. 262, 115121.
Paradies, G., Paradies, V., Ruggiero, F.M., Petrosillo, G., 2019. Role of cardiolipin in mitochondrial function and dynamics in health and disease: molecular and pharmacological aspects. Cells 8.
Paradies, G., Paradies, V., Ruggiero, F.M., Petrosillo, G., 2014. Oxidative stress, cardiolipin and mitochondrial dysfunction in nonalcoholic fatty liver disease. World J. Gastroenterol. 20, 14205–14218.
Savic, D., Hodson, L., Neubauer, S. & Pavlides, M. The Importance of the Fatty Acid Transporter L-Carnitine in Non-Alcoholic Fatty Liver Disease (NAFLD). Nutrients vol. 12 at https://doi.org/10.3390/nu12082178 (2020).
Enooku, K., et al., 2019. Altered serum acylcarnitine profile is associated with the status of nonalcoholic fatty liver disease (NAFLD) and NAFLD-related hepatocellular carcinoma. Sci. Rep. 9, 10663.
Roth, K., et al., 2021. Exposure to a mixture of legacy, alternative, and replacement per- and polyfluoroalkyl substances (PFAS) results in sex-dependent modulation of cholesterol metabolism and liver injury. Environ. Int. 157, 106843.
Sedik, A.A., et al., 2024. Lauric acid attenuates hepato-metabolic complications and molecular alterations in high-fat diet-induced nonalcoholic fatty liver disease in rats. Toxicol. Mech. Methods 34, 454–467.
Merry, T.L., et al., 2020. Mitochondrial-derived peptides in energy metabolism. Am. J. Phys. Endocrinol. Metab. 319, E659–E666.
India-Aldana, S., et al., 2023. PFAS exposures and the human metabolome: a systematic review of epidemiological studies. Curr. Pollut. Reports 9, 510–568.
Addicks, G.C., et al., 2025. Identification of four mechanisms of toxicity for per- and polyfluoroalkyl substances through transcriptomic profiling in human liver spheroids exposed to 24 PFAS. Toxicol. Sci. kfaf075. https://doi.org/10.1093/toxsci/kfaf075.
Nishi, K., et al., 2023. Branched-chain keto acids inhibit mitochondrial pyruvate carrier and suppress gluconeogenesis in hepatocytes. Cell Rep. 42, 112641.
Walejko, J.M., et al., 2021. Branched-chain α-ketoacids are preferentially reaminated and activate protein synthesis in the heart. Nat. Commun. 12, 1680.
Gebreab, K.Y., et al., 2020. Comparative toxicometabolomics of perfluorooctanoic acid (PFOA) and next-generation perfluoroalkyl substances. Environ. Pollut. 265, 114928.
Zhang, Y. et al. Role of Selenoproteins in Redox Regulation of Signaling and the Antioxidant System: A Review. Antioxidants (Basel, Switzerland) 9, (2020).
Nguyen, T.V., Trang, P.N., Kumar, A., 2024. Understanding PFAS toxicity through cell culture metabolomics: current applications and future perspectives. Environ. Int. 186, 108620.
Liu, C. et al. Perfluoroalkyl and Polyfluoroalkyl Substances (PFAS) and Vitamin Metabolism: A Nutritional Perspective on an Emerging Environmental Health Issue. Nutrients vol. 17 at https://doi.org/10.3390/nu17101660 (2025).
Qi, Q., et al., 2023. Per- and polyfluoroalkyl substances activate UPR pathway, induce steatosis and fibrosis in liver cells. Environ. Toxicol. 38, 225–242.
Charni-Natan, M., Aloni-Grinstein, R., Osher, E., Rotter, V., 2019. Liver and steroid hormones-can a touch of p53 make a difference? Front. Endocrinol. (lausanne) 10, 374.
Guo, P., et al., 2022. Non-targeted metabolomics and associations with per- and polyfluoroalkyl substances (PFAS) exposure in humans: a scoping review. Environ. Int. 162, 107159.
Maltais-Payette, I., et al., 2025. Associations between circulating amino acids and metabolic dysfunction-associated steatotic liver disease in individuals living with severe obesity. Physiol. Rep. 13, e70171.
Zhang, Y., et al., 2023. Folate concentrations and serum perfluoroalkyl and polyfluoroalkyl substance concentrations in adolescents and adults in the USA (National Health and Nutrition Examination Study 2003-16): an observational study. Lancet. Planet. Heal. 7, e449–e458.
Brown, M.V., Compton, S.A., Milburn, M.V., Lawton, K.A., Cheatham, B., 2013. Metabolomic signatures in lipid-loaded HepaRGs reveal pathways involved in steatotic progression. Obesity (Silver Spring) 21, E561–E570.
Lee, S., Jin, M.H., Yoon, J.-H., 2024. The contribution of vitamin D insufficiency to the onset of steatotic liver disease among individuals with metabolic dysfunction. Sci. Rep. 14, 6714.
Yu, N., et al., 2016. Effects of perfluorooctanoic acid on metabolic profiles in brain and liver of mouse revealed by a high-throughput targeted metabolomics approach. Sci. Rep. 6, 23963.

Vujic, E., Ferguson, S.S., Brouwer, K.L.R., 2024. Effects of PFAS on human liver transporters: implications for health outcomes. Toxicol. Sci. 200, 213–227.
Liu, D., et al., 2021. Squalene epoxidase induces nonalcoholic steatohepatitis via binding to carbonic anhydrase iii and is a therapeutic target. Gastroenterology 160, 2467–2482.e3.
Veliova, M., Petcherski, A., Liesa, M., Shirihai, O.S., 2020. The biology of lipid droplet-bound mitochondria. Semin. Cell Dev. Biol. 108, 55–64.